remote sensing

Article

Inversion of Forest above Ground Biomass in Mountainous Region Based on PolSAR Data after Terrain Correction: A Case Study from Saihanba, China

Yonghui Nie , Yifan Hu, Rula Sa and Wenyi Fan *

Key Laboratory of Sustainable Forest Ecosystem Management (Ministry of Education), School of Forestry, Northeast Forestry University, Harbin 150040, China; nieyonghui@nefu.edu.cn (Y.N.); yifan_hu2021@nefu.edu.cn (Y.H.); sarula@nefu.edu.cn (R.S.)
* Correspondence: fanwy@nefu.edu.cn; Tel.: +86-139-4605-5384

Abstract: Accurate retrieval of forest above ground biomass (AGB) based on full-polarization synthetic aperture radar (PolSAR) data is still challenging for complex surface regions with fluctuating terrain. In this study, the three-step process of radiometric terrain correction (RTC), which includes polarization orientation angle correction (POAC), effective scattering area correction (ESAC), and angular variation effect correction (AVEC), is adopted as the technical framework. In the ESAC stage, a normalized correction factor is introduced based on local incidence angle and radar incidence angle to achieve accurate correction of PolSAR data information and improve the inversion accuracy of forest AGB. In order to verify the validity and robustness of this research method, the full-polarization SAR data of ALOS-2 and the ground measured AGB data collected in the Saihanba research area in 2020 were used for experiments. Our findings revealed that in the ESAC phase, the introduction of the normalized correction factor can effectively eliminate the ESA phenomenon and improve the correlation coefficients of the backscatter coefficient and AGB. Taking the data of 25 July 2020 as an example, ESAC increases the correlation coefficients between AGB and the backscattering coefficients of HH, HV, and VV polarization channels by 0.343, 0.296, and 0.382, respectively. In addition, the RTC process has strong robustness in different AGB statistical models and different date PolSAR data.

Keywords: AGB inversion; spaceborne SAR; ALOS-2; L-band; topographic correction; ESAC; backscattering coefficient

check for updates

Citation: Nie, Y.; Hu, Y.; Sa, R.; Fan, W. Inversion of Forest above Ground Biomass in Mountainous Region Based on PolSAR Data after Terrain Correction: A Case Study from Saihanba, China. *Remote Sens.* **2024**, *16*, 846. https://doi.org/10.3390/rs16050846

Academic Editors: Bogdan Andrei Mihai and Marcel Torok

Received: 17 January 2024
Revised: 22 February 2024
Accepted: 26 February 2024
Published: 28 February 2024

1. Introduction

As the main body of the terrestrial ecosystem and the largest organic carbon reservoir [1,2], forests play an irreplaceable role in regulating the global carbon cycle [3] and mitigating the global climate change crisis [4]. However, accurate inversion of forest above ground biomass (AGB) remains challenging, especially in regions with complex topography, which greatly limits sustainable mountain forest stand management and the quantification of carbon sequestration by AGB [5,6]. Synthetic aperture radar (SAR) is an advanced remote sensing observation technology for the earth, and because of its active remote sensing and microwave penetration characteristics, it has all-time, all-weather working capability [7,8]. Therefore, it can effectively avoid the problems of time-consuming and labor-intensive discontinuity in ground measurement [9,10], the problems of optical remote sensing being easily restricted by climate factors and the bottleneck of saturation point [11–13], and the limitations of light detection and ranging (LiDAR) remote sensing being limited in scale and high in economic cost [14], which are conducive to long-term, continuous, and macroscopic observation of large areas. However, as SAR is a side-looking radar imaging system that judges oblique distance based on echo time, SAR data are not only affected by system parameters (wavelength, radar incidence angle, polarization mode) but also limited by surface characteristics (complex dielectric constant, terrain slope, surface roughness). The topographic factor interferes with SAR data especially seriously, and the geometric deformation and radiation distortion caused by it lead to the serious deviation of the backscattering coefficient of ground objects [15], thus restricting the reliability of forest AGB inversion based on the backscattering coefficient of SAR images. Therefore, it is very important to explore the technique of retrieving AGB in mountainous forest areas with complex terrain based on the SAR dataset. Since different AGB inversion schemes have different topographic correction processes, the inversion technology of aboveground biomass is first analyzed. At present, AGB estimation techniques based on SAR data can be divided into: (1) Statistical modeling method based on SAR characteristic parameters (including backscattering coefficient [16–19], polarization decomposition parameter [20,21], interference coherence [22–24], and tomographic vertical structure parameter [25]) and (2) forest canopy height extracted from interferometric SAR (InSAR) [26–28], polarimetric interferometric SAR (PolInSAR) [29–31] and tomographic SAR (TomoSAR) [32]; and then indirect AGB estimation using an allometric equation [33,34]. Among them, the accuracy of indirect inversion of forest AGB based on an allometric equation is heavily dependent on the inversion accuracy of the growth equation and forest canopy height. However, the accurate acquisition of forest height, interference coherence, and tomographic vertical structure parameters depends on InSAR, PolInSAR, TomoSAR, and other related technologies, which are mostly used for airborne data but seldom studied for spaceborne data, are not mature enough, and have many limitations. However, polarimetric SAR (PolSAR) technology can obtain multi-polarization scattering information about ground objects, so it has been widely used in estimating forest AGB [35–37]. In addition, the forest AGB model constructed based on SAR characteristic parameters is divided into a parametric model and a non-parametric model, among which the non-parametric model has greater flexibility and adaptability because it does not depend on specific functional forms [38,39]. However, the parameter model is easy to explain and understand because of its clear mathematical formula, and the parameter estimation can be relatively fast and the calculation efficiency is high, so it has a wide range of applications in the estimation of forest AGB. The method of retrieving AGB based on the backscattering coefficient of PolSAR data is relatively mature and widely used, so this study focuses on analyzing the influence of terrain on the parameter model based on the backscattering coefficient to retrieve AGB. For full-polarization SAR data, the backscattering coefficient method is to extract the backscattering intensity of different polarization channels after proper preprocessing of PolSAR data and establish a univariate or multivariate statistical model about AGB [40]. However, PolSAR data are affected by topographic factors, resulting in geometric deformation and radiation distortion of SAR images [41]. Among them, the correction of geometric distortions (including foreshortening, layover, and shadow) can be done during geocoding of terrain correction (GTC) [42]. In addition, the impact of topographic factors on radiation distortion of PolSAR data mainly includes three aspects [43]: (1) The shift of polarization orientation angle (POA) results in a change in polarization state; (2) the difference in effective scattering area (ESA) leads to a change in intensity information of target scattering matrix elements; (3) changes in the scattering mechanism and penetration depth are caused by the angular variation effect (AVE). For sloping ground, the POA will shift [44]. As the parameters of the polarization elliptic equation, POA and ellipse angle can be used to describe the polarization state of any polarized electromagnetic wave [45]. Therefore, the polarization state of a polarized electromagnetic wave will change correspondingly with the change in POA. As the key to polarization orientation angle correction (POAC), the extraction of POA currently has four methods: Based on the polarization response method [46], based on polarization decomposition method [47], based on the external DEM method [48], and based on the circular polarization covariance matrix method [48]. Among them, the estimation method based on circular polarization covariance matrix has the best adaptability, a simple calculation process, and an optimal comprehensive effect [49]. Subsequently, correction factors constructed by POA are used to compensate for different forms of polarization information [48,50,51], such as the complex Sinclair scatter matrix

(S2), the three-dimensional polarization coherency matrix (T3), or the three-dimensional polarization covariance matrix (C3). It is worth noting that the compensation for POA is only for full-polarization SAR data [48]. Effective scattering area correction (ESAC) is a system-level correction of the SAR image based on the geometric relationship of the SAR image and is a necessary step in radiation terrain correction. For ground units with only different slopes (even with geometric correction), the existence of a topographic slope will lead to differences in the projected area (effective scattered echo information) of their positive plane; for example, the echo intensity of the front slope is greater than that of the back slope [43]. At present, there are four ESAC methods: Local incidence angle method [52,53] and projection angle method [54] under ground distance geometry, and σ area integration method and γ area integration method under oblique distance geometry [55,56], which can correct PolSAR information such as backscattering coefficient or C3 or T3. Angular variation effect correction (AVEC) takes into account factors such as the penetration depth of radar waves and the interaction mechanism between the radar waves and vegetation, which is a more precise correction method for vegetation areas with certain penetration. Therefore, for forested areas, further AVEC is required on the basis of ESAC. AVEC usually uses the semi-empirical correction equation of the cosine of the local incidence angle to the nth power [57], where the n value depends on the polarization mode and the structural characteristics of the vegetation canopy and is usually given based on prior knowledge. Subsequently, a variety of methods for the value of n have appeared [52,57–60], but they are still difficult to apply because they cannot be separated from prior knowledge. However, a new iterative method [43] based on the minimum correlation coefficient between the backscattering coefficient and the local incidence angle after AVEC realizes the adaptive determination of the optimal n value for different polarized channels.

Compared to a process that does not consider or does not adequately consider topographic correction [38,61], radiative terrain correction for PolSAR data is a combination of three aspects of terrain correction [50,59,60,62,63], of which the most comprehensive radiometric terrain correction (RTC) process is one that includes all three aspects (POAC, ESAC, and AVEC) [43,64,65]. However, in terms of ESAC, the cross-sectional area of radar scattering is only applicable to a single scattering target (the target object is smaller than the irradiation range), and the scattered signal of the resolution unit for distributed scatterers (such as forests) is the result of coherent superposition of the scattered signal of each single scatterer, so the backscattering coefficient is commonly used to describe the scattering ability of ground objects based on statistical methods. Three different backscattering coefficients can be defined according to the area of the effective scattering element: the backscattering coefficient of the imaging surface (β^0), the backscattering coefficient of the ground regardless of the terrain (σ^0), and the backscattering coefficient of the isophase surface (γ^0) [55,66]. When ESAC's object is σ^0, it essentially converts σ^0 to γ^0 in relation to the topographic factor. However, when the ESAC object is C3 or T3, it is not appropriate to directly use the ESAC factors applied to σ^0 as the ESAC factors of C3. Because, on flat ground with no topographic slope, C3 does not require topographic correction; that is, the correction factor should equal 1.0. Therefore, it is necessary to introduce a new ESAC factor to realize real terrain correction rather than simple conversion. In addition, the robustness of the RTC process to different AGB inversion models and different SAR data has not been fully evaluated.

This study aims to achieve three goals: (1) In order to deal with the problem that the impact of terrain on SAR data is not considered or not fully considered, we fully consider the impact (including POA, ESA, and AVE) of terrain on PolSAR data in AGB inversion based on the backscattering coefficient method; (2) to solve the problem that PolSAR data needs more accurate terrain correction rather than simple conversion, we introduced and verified the effectiveness of the ESAC normalized correction factor; and (3) to evaluate the robustness of the RTC process under different AGB models and SAR data of different dates, because it has not been adequately evaluated.

2. Materials

2.1. Study Area

The study area was located in Saihanba Forest Farm (116°53′~117°43′E, 41°55′~42°35′N, Figure 1) in the northernmost part of Weichang County, Hebei Province, China, with an altitude of 1010~1940 m. The main reasons for choosing this test site are as follows: (1) First of all, its vegetation types are diverse, including deciduous coniferous forest, evergreen coniferous forest, broad-leaved forest, scrub, grassland, and swamp, and its surface is complex, especially since the forest area contains not only flat woodland but also steep mountain terrain, with slope angles of up to 55.47° in some places (Figure A3b, Appendix A), and the slope is widely distributed. It is beneficial for comparative study of complex terrain; (2) Saihanba Forest is the largest artificial forest in the world [67], with an area of about 93,461 hectares, which has a large test forest area and is easy to collect real test data manually; (3) Saihanba Forest Farm, located at the intersection of the Inner Mongolia Plateau and the northern mountains of Hebei, is an ecological replacement zone of typical forests in northern China [68], which is representative of the region and shoulders the important mission of water source protection and ecological security.

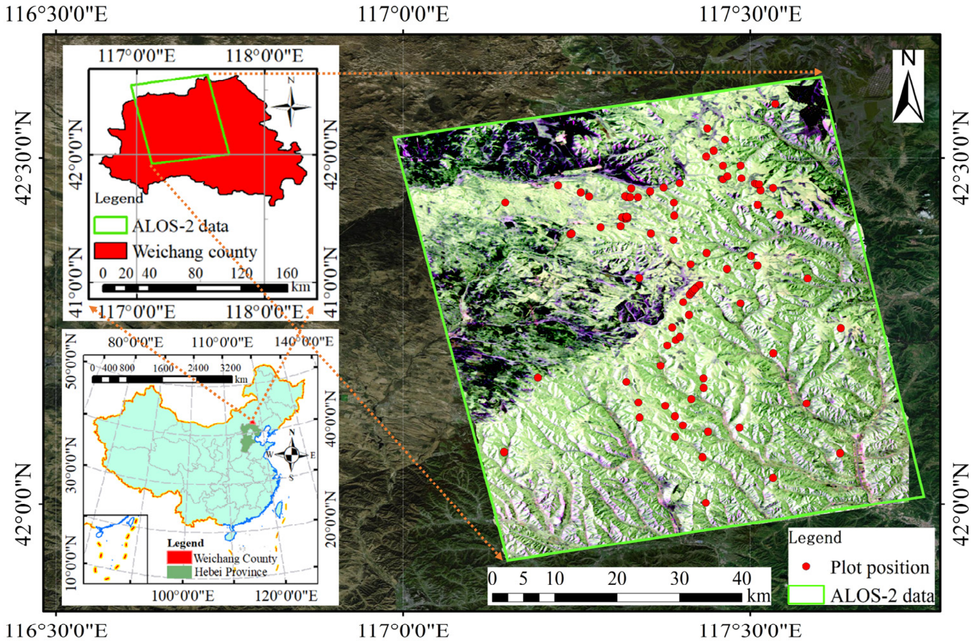

Figure 1. Saihanba study area: The lower figure on the right is the location of Saihanba Forest Farm in provinces and counties in China; the upper figure on the right is the spatial location of ALOS-2 data; the left figure is the Pauli RGB image (R: ∣HH-VV∣, G: ∣HV∣, B: ∣HH + VV∣,) based on PolSAR data and the location of measured samples; and the basemap is the optical image of Tianditu.

2.2. PolSAR Dataset

The PolSAR dataset was obtained by the advanced land observing satellite-2 (ALOS-2) developed by the Japan Aerospace Exploration Agency (JAXA). It includes L-band full-polarization Single Look Complex (SLC) observation data dated 11 July 2020, 25 July 2020, 8 August 2020, 5 September 2020, and 19 September 2020 (Figure A1, Appendix A), in which images of different dates have the same main parameters (Table 1). The main reasons for selecting this dataset as remote sensing data for AGB inversion in mountainous forest areas are as follows: (1) Compared with single-polarization and multi-polarization, full-polarization data can be used for more accurate inversion of forest above-ground biomass due to its more comprehensive polarization channel information; (2) the selection of full-polarization SAR data is helpful to comprehensively study and control the error caused by terrain factors, because the influence of terrain on full-polarization SAR data is different from that of non-full-polarization SAR data; (3) the L-band is more penetrating than C-band, so it can obtain forest structure information more accurately and can have higher sensitivity to SAR data and AGB, but ALOS-2 is currently the only spaceborne SAR satellite using L-band frequencies.

Table 1. The main parameters of the PolSAR dataset.

Parameter	Value
Observation direction	Right looking
Orbit direction	Ascending
Observation mode	HBQ
Data formats and processing level	CEOS level 1.1
Observation date of scene center	27.8054°
Radar wavelength	0.2424525 m
Range resolution	2.860844 m
Azimuth resolution	2.642742 m
Length of range direction	49.8 km
Length of azimuth direction	69.3 km
Range pixel	8392
Azimuth pixel	26,105

2.3. Field Data

In order to be consistent with the acquisition time and scanning area of SAR images, we started a 20-day field survey project in the Saihanba research area covered by SAR data from 1 August 2020. A total of 179 temporary sample plots (Figure 1) were set up, of which 28 were systematically sampled on a one-kilometer grid and 151 with relatively uniform and discrete distribution were selected by investigating the tree species, forest types, understory conditions, topographic slope, thinning density, and forest height of the plots, which can make the samples better represent the overall situation of the forest area. In the layout of plots (Figure A2, Appendix A), each plot avoids roads, rivers, forest edges, large empty windows, and felled survey lines, chooses a representative central position within the same stand, and then uses handheld GPS (Unistrong RTK-G10, Unistrong, Beijing, China) to locate the central point position (ensure that the coordinate error of the central point of the plot is within 10 cm). Then, the four corner points 17.32 m away from the center point were located along the four positive directions determined by the compass, and then a diamond shaped plot of 24.49 m × 24.49 m with an area of 0.06 ha was enclosed. Subsequently, the height and diameter at breast height (DBH) of each tree larger than 5.0 cm were measured by an ultrasonic height measuring instrument (Vertex IV, Haglöf Sweden AB, Långsele, Sweden) and a diameter ruler, respectively, and plot information such as tree species, plant number and slope were recorded. Finally, the data were summarized into a table, and the sample site data were standardized to eliminate sample plots with missing values and outliers. The measured AGB can be obtained by calculating the biomass of individual trees in the plot according to the allometric equation of different tree species (Table 2) and adding it up according to Equation (1).

$$AGB_j = \sum_{i=1}^{m} W_i/1000 \times S \tag{1}$$

where AGB_j is the AGB (t/ha) of the jth sample plot, m is the number of trees in the plot, W_i is the AGB of the ith tree (kg), and S is the area of the sample plot (S = 0.06 ha).

Table 2. Table of allometric equations of different tree species.

Tree Species	Allometric Growth Equation	Ref
Larix principis-rupprechtii	$W = 0.1431 \cdot DBH^{2.2193}$	[69]
Betula platyphylla	$W = 0.0330 \cdot DBH^{2.9314}$	[70]
Pinus sylvestris var. *mongolica*	$W = 0.0930 \cdot DBH^{2.3429}$	[71]
Pinus tabuliformis	$W = 0.0520 \cdot DBH^{2.5830}$	[72]
Acer truncatum	$W = 0.1260 \cdot DBH^{2.3830}$	[73]

Note: *W* and *DBH* were AGB (kg) and diameter at breast height of a single tree in the plot, respectively.

In order to enhance the clarity and transparency of the study, we provide statistical details of the field data in Table 3.

Table 3. Sample plot AGB statistics.

Data	Min (t/ha)	Max (t/ha)	Mean (t/ha)	SD (t/ha)
Train (*N* = 134)	36.39	163.88	103.86	32.39
Test (*N* = 45)	23.74	166.58	94.93	40.87

Note: SD is standard deviation, *N* is the number of sample plots.

2.4. SRTM DEM Data

The Shuttle Radar Topography Mission (SRTM) digital elevation model (DEM) data (Figure A3a, Appendix A) with a resolution of 30 m were used to assist PolSAR data to complete geocoding and topographic correction factor extraction.

3. Methods

The processing process framework of this study (Figure 2) mainly includes: (1) Pre-processing (see Section 3.2 for details) SLC 1.1 level data of PolSAR dataset, including cross-channel SNR correction, Faraday rotation correction, calibrate, multilooking, and polarimetric speckle filtering. (2) In order to verify the validity of the RTC process of introducing the normalized correction factor in the ESAC stage in the inversion of mountain forest AGB, it is set and assumed that no topographic influence exists in the blank control group and no radiometric terrain correction (NRTC) is performed, but the range Doppler terrain correction is completed after pre-processing to achieve geocoding. For the experimental group, the influence of complex terrain should be fully considered, and POAC, range Doppler terrain correction, ESAC, and AVEC should be completed after pretreatment. (3) In order to verify the robustness of the RTC process in different inversion models and PolSAR data of different dates, the backscattering coefficients were extracted based on the data of the experimental group and the control group, respectively, and the fitting and evaluation of different models were carried out combined with the measured AGB, and the influence of different RTC stages on the AGB inversion of mountain forest was analyzed. Then, based on the most stable model, the influence of the RTC process on the AGB inversion in the data of different dates is analyzed. (4) Finally, the AGB data for the whole study area are obtained based on the average value of AGB obtained from the data inversion of five dates. The following sections give the necessary theories and related formulas for each stage in the flow chart in more detail.

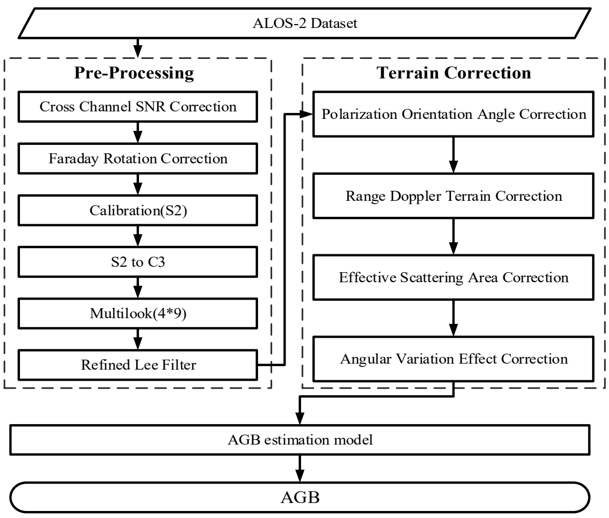

Figure 2. The flowchart of the proposed AGB mapping scheme.

3.1. Polarization Scattering Descriptors

Under the horizontal/vertical linear polarization basis, the full-polarization SAR data can be characterized by the 2 × 2 complex Sinclair scatter matrix (S2), which contains ground object scattering information:

$$S2 = \begin{bmatrix} S_{HH} & S_{HV} \\ S_{VH} & S_{VV} \end{bmatrix} \tag{2}$$

In order to conduct a more accurate analysis of distributed targets and because the single station data meet reciprocity, that is, $S_{HV} = S_{VH}$, polarization coherency matrix (T3) and the polarization covariance matrix (C3) are two second-order statistical matrices used to characterize scattering targets. In addition, a special unitary transformation (SU) can be used to convert T3 and C3 to each other. The equation for C3 is as follows:

$$C3 = \begin{bmatrix} \left\langle |S_{HH}|^2 \right\rangle & \sqrt{2}\left\langle S_{HH}S_{HV}^* \right\rangle & \left\langle S_{HH}S_{VV}^* \right\rangle \\ \sqrt{2}\left\langle S_{HH}S_{HV}^* \right\rangle & 2\left\langle |S_{HV}|^2 \right\rangle & \sqrt{2}\left\langle S_{HV}S_{VV}^* \right\rangle \\ \left\langle S_{HH}S_{VV}^* \right\rangle & \sqrt{2}\left\langle S_{HV}S_{VV}^* \right\rangle & \left\langle |S_{VV}|^2 \right\rangle \end{bmatrix} \tag{3}$$

where <·> denotes multi-look averaging. * denotes conjugate matrices.

3.2. PolSAR Data Pre-Processing

In this study, the Sentinel Application Platform (SNAP_v9.0.0) software developed by the European Space Agency was used to preprocess PolSAR data: (1) Cross-channel SNR correction to eliminate system errors; (2) Faraday rotation correction to remove the Faraday rotation effect caused by the ionosphere; (3) Equation (5) is used to establish the exact relationship between SAR data and backscattering information of ground objects, and the resulting data of radiometric calibration is saved as S2 matrix, where Equation (5) can be derived according to radiometric calibration Equation (4) applicable to 1.1 ALOS-2 data; (4) the S2 matrix after radiation calibration is converted into C3 matrix to facilitate RTC processing; (5) by using 4 × 9 (range × azimuth) multi-look averaging, it is consistent with the size of the plot and the noise reduction of the speckle is realized; (6) a refined LEE filter with a number of looks of 1 and a window size of 7 × 7 was used to denoise the PolSAR data again; (7) range Doppler terrain correction (TC) is performed on the NRTC data so that the images can be encoded from the SAR coordinate system to the geographic coordinate system while the geometric distortion caused by the terrain is corrected. SRTM's 30 m resolution DEM is required for this operation. In addition, because POAC processing is ideally completed before TC, for data requiring RTC processing, its preprocessing only needs to be a refined LEE filter, and its TC processing is placed after POAC.

The radiometric calibration equation applicable to the 1.1 ALOS-2 data is shown in Equation (4), and the equation for radiometric calibration of S2 scattering matrix can be derived Equation (5):

$$\sigma_{slc}^{0} = 10 \cdot \log_{10}\left\langle I^2 + Q^2 \right\rangle + CF_1 - A \tag{4}$$

where ${\sigma^0}_{slc}$ is the backscattering coefficient after radiation calibration; I and Q represent the real and imaginary parts of SLC 1.1 products, respectively. CF_1 is −83.0 dB; the value of A is 32.0 dB.

$$I_{cal} = \frac{I}{10^{5.75}}; Q_{cal} = \frac{Q}{10^{5.75}} \tag{5}$$

where I_{cal} and Q_{cal} are the real and imaginary parts of the S2 scattering matrix after radiation calibration.

3.3. Radiation Terrain Correction

3.3.1. Polarization Orientation Angle Correction

The polarization orientation angle (POA) is the angle between the major axis of the polarization ellipse and the horizontal axis (Figure A4b, Appendix A). POA will shift when there is a slope on the flat surface. The offset angle (mainly caused by azimuth slope) can be equivalent to the rotation angle (η) of the scattered target image surface caused by terrain with respect to the radar line of sight (Figure A4a, Appendix A).

In order to compensate for the deviation of POA caused by the terrain. (1) Firstly, POA is extracted based on the calculation of Equation (6) of the circular polarization method [49]; (2) Subsequently, in order to facilitate the calculation of the backscattering coefficient, Equation (7) is used to correct C3.

$$\eta = \frac{1}{4}\left[-1 \times Arg\left(\left\langle \frac{-4\mathrm{Re}\left\langle (S_{HH} - S_{VV})S_{HV}^{*}\right\rangle}{-\left\langle |S_{HH} - S_{VV}|^{2}\right\rangle + 4\left\langle |S_{HV}|^{2}\right\rangle}\right\rangle\right) + \pi\right] \tag{6}$$

where η is the polarization azimuth; $Arg(\cdot)$ is a phase function. When $\eta > \pi/4$, $\eta = \eta - \pi/2$.

$$\begin{aligned} C_{3\_POAC} &= U_{3(\eta)} C_3 U_{3(\eta)}^{-1} \\ U_{3(\eta)} &= \frac{1}{2}\begin{bmatrix} 1+\cos(2\eta) & \sqrt{2}\sin(2\eta) & 1-\cos(2\eta) \\ -\sqrt{2}\sin(2\eta) & 2\cos(2\eta) & \sqrt{2}\sin(2\eta) \\ 1-\cos(2\eta) & -\sqrt{2}\sin(2\eta) & 1+\cos(2\eta) \end{bmatrix} \end{aligned} \tag{7}$$

where *C3* and C_{3_POAC} are C3 before and after POAC, respectively. η is the polarization orientation angle (POA).

3.3.2. Effective Scattering Area Correction

The effective scattering area is the projected area of the actual ground unit in the equal-phase plane. However, due to the difference in terrain slope, the ground unit of the same SAR data in the geographical coordinate system corresponds to different effective scattering areas (Figure A5, Appendix A). Therefore, it is necessary to correct the area effect of SAR data based on flat ground to eliminate the influence of terrain slope on scattering information.

For distributed targets, the backscattering coefficient is usually used to describe the scattering ability of ground objects. Depending on the area of the effective scattering unit, three different backscattering coefficients can be defined:

$$\langle \sigma \rangle = \beta^0 \cdot A_\beta = \sigma^0 \cdot A_\sigma = \gamma^0 \cdot A_\gamma \tag{8}$$

where σ is the radar scattering cross-section; <·> is multi-look averaging; β^0, σ^0, and γ^0 are respectively the backscattering coefficients of the imaging plane, horizontal plane, and equiphase plane; A_β, A_σ, and A_γ are the effective scattering unit areas of the imaging plane, horizontal plane, and equiphase plane, respectively.

At the same time, for the same pixel, there is a geometric relationship under the two conditions of assuming flat ground and considering slope:

$$\beta^0 = \frac{\sigma^0}{\sin\left(\theta_{ref}\right)} = \frac{\sigma^0_{slope}}{\sin(\theta_{loc})} \tag{9}$$

where σ^0 is the backscattering coefficient assumed to be flat ground; ${\sigma^0}_{slope}$ is the backscattering coefficient considering terrain conditions; θ_{loc} is the local incidence angle; θ_{ref} is the radar incidence angle.

Thus, the exact expression of the backscattering coefficient and C3 matrix after ESAC can be obtained:

$$\begin{aligned} \sigma^0_{ESAC} &= \sigma^0 \cdot F_{ESAC} = \sigma^0 \cdot \frac{\sin(\theta_{loc})}{\sin(\theta_{ref})} \\ C_{3\_ESAC} &= C_3 \cdot F_{ESAC} = C_3 \cdot \frac{\sin(\theta_{loc})}{\sin(\theta_{ref})} \end{aligned} \tag{10}$$

where $\sigma^0{}_{ESAC}$ and $C3_{\_ESAC}$ are the backscattering coefficients and the C3 matrix after ESAC, respectively. F_{ESAC} is the correction factor of ESAC. *C3* refers to the C3 matrix without ESAC, and in this study, it specifically refers to the C3 matrix after POAC and TC.

3.3.3. Angular Variation Effect Correction

The angle effect refers to the phenomenon that the local incidence angle changes due to the topography, thus affecting the scattering mechanism of the target surface object (Figure A6, Appendix A). For forest and other vegetation areas with complex structures, local topography not only affects the effective scattering area of each pixel but also its physical scattering mechanism, resulting in changes in backscattering information [57].

Changes in the backscattering coefficient caused by AVE are usually corrected using the cosine model:

$$\sigma^0_{AVEC}(n) = \sigma^0 \cdot k(n) = \sigma^0 \cdot \left(\frac{\cos\theta_{ref}}{\cos\theta_{loc}}\right)^n \tag{11}$$

where σ^0 and $\sigma^0{}_{AVEC}(n)$ are the backscattering coefficients before and after AVEC; *K(n)* is the correction factor function of AEVC with respect to n.

As the key to the calculation of *K(n)*, the estimation of the n value can be automatically calculated by Equation (12): (1) firstly, the correlation coefficient between the local incidence angle and the backscattering coefficients of different polarization channels corrected by AVEC when n takes different values is calculated; (2) then, the optimal n value is determined by calculating the minimum value of the absolute value of the correlation coefficient obtained.

$$n_{pq} = argmin\left\{f_{(n)}\right\} = argmin\left\{\left|\rho\left(\theta_{loc}, \sigma^0_{AVEC}\right)\right|\right\} \tag{12}$$

where (p, q) = (H, V) is the polarization mode of incidence and scattering of electromagnetic waves; n_{pq} is the optimal n value of different polarization channels; *argmin{·}* is the operation that takes the minimum value; $\sigma^0{}_{AVEC}$ is the backscattering coefficient after AVEC; *f(n)* is the absolute value of the correlation coefficient between $\sigma^0{}_{AVEC}$ and the local incidence angle θ_{loc}; $\rho(\cdot)$ is the correlation coefficient function.

Assuming that the optimal n values of different polarized channels are n_{HH}, n_{HV}, and n_{VV}, the correction equation and correction factor corresponding to the C3 matrix are as follows:

$$\begin{aligned} &C_{3\_AVEC} = C_3 \odot K \\ &K = \begin{bmatrix} k(n_{HH}) & k\left(\frac{n_{HH}+n_{HV}}{2}\right) & k\left(\frac{n_{HH}+n_{VV}}{2}\right) \\ k\left(\frac{n_{HH}+n_{HV}}{2}\right) & k(n_{HV}) & k\left(\frac{n_{HV}+n_{VV}}{2}\right) \\ k\left(\frac{n_{HH}+n_{VV}}{2}\right) & k\left(\frac{n_{HV}+n_{VV}}{2}\right) & k(n_{VV}) \end{bmatrix} \end{aligned} \tag{13}$$

where $\odot$ a is the Hadamard product.

In practical application, since different surface object types correspond to different optimal n values, AGB in forest areas is the core research object, and the existence of non-forest will lead to a reduction in correlation, it is necessary to first classify forest and non-forest surface object types. In this study, Freeman three-component decomposition and a Wishart unsupervised classifier were used to classify PolSAR data, and the forest cover area was extracted as a mask file. Finally, the C3 matrix was masked based on the mask file, and then AEVC was carried out.

3.4. AGB Inversion Model

In order to evaluate the impact of each stage of RTC on the AGB estimation performance and the adaptability to different models, five AGB inversion models (Equation (14)) were constructed and tested. The basic models are model 0 (M0) and model 1 (M1). After preliminary experiments, it was found that M1 was much better than M0. Meanwhile, in order to deal with the heteroscedasticity problem shown by AGB data, that is, the error variance was not constant over all observations, we used a logarithmic regression model to estimate AGB. Therefore, model 2 (M2) was constructed with the logarithmic form of M1. The backscattering intensity of elements on the diagonal of the C3 matrix in intensity units is taken as the variable of the estimation model.

$$\begin{cases} M0: AGB = a_0 + a_1 \cdot \sigma^0_{pq} \\ M1: AGB = a0 \cdot \left(\sigma^0_{pq}\right)^{a_1} \\ M2: \ln(AGB) = a_0 + a_1 \cdot \ln\left(\sigma^0_{pq}\right) \\ M3: \ln(AGB) = a_0 + a_1 \cdot \ln\left(\sigma^0_{pq}\right) + a_2 \cdot \left(\ln\left(\sigma^0_{pq}\right)\right)^2 \\ M4: \ln(AGB) = a_0 + a_1 \cdot \ln\left(\sigma^0_{HH}\right) + a_2 \cdot \ln\left(\sigma^0_{HV}\right) + a_3 \cdot \ln\left(\sigma^0_{VV}\right) \end{cases} \tag{14}$$

where (p, q) = (H, V) is the polarization mode of incidence and scattering of electromagnetic waves; ${\sigma^0}_{pq}$ is the backscattering coefficient under different polarization channels; a_0, a_1, and a_2 are the model coefficients.

3.5. Model Validation

In order to ensure the stability of the model, based on 179 measured plot data, the random separation verification method was adopted to conduct stratified random sampling according to biomass level and slope size. Seventy-five percent was selected as modeling samples (134 training data) for model fitting, and the remaining 25% was selected as test samples (45 verification data) for model testing. Evaluate the goodness of fit between the measured data and the model prediction (AGB) using three parameters, including the coefficient of determination (R^2, Equation (15)), root mean square error (RMSE, Equation (16)) and relative root mean squared error (RRMSE, Equation (17)).

$$R^2 = 1 - \frac{\sum_{i=1}^{N}(y_i - \hat{y}_i)^2}{\sum_{i=1}^{N}(y_i - \overline{y})^2} \tag{15}$$

$$RMSE = \sqrt{\frac{1}{n}\sum_{i=1}^{N}(y_i - \hat{y}_i)^2} \tag{16}$$

$$RRMSE = (RMSE/\overline{y}) \times 100\% \tag{17}$$

where N is the sample size, y_i represents the true observed value, $\overline{y}$ represents the average of the true observed value, and $\hat{y}_i$ represents the predicted value.

4. Results

In this section, we (1) implement the processing workflow shown in Figure 2 and demonstrate the correction factors for the three stages in the RTC; (2) the correction effect of RTC at each stage was analyzed qualitatively and quantitatively using Pauli RGB images and backscattering coefficient images before and after RTC; (3) the effectiveness of RTC is validated through examining the correlation between the backscattering coefficient and the measured AGB; (4) the robustness of RTC is verified by analyzing the performance of terrain correction results in different statistical models and SAR data of different dates. In the following sections, we take the data of a selected date (25 July 2020) as an example to show the core results of the study in detail. Meanwhile, all the results are presented in the geographic coordinate space for convenience of comparison.

4.1. Correction Factors of Radiometric Terrain Correction

According to the image (Figure 3a) of the polarization azimuth shift caused by terrain, the POA value is distributed between −45° and +45°, and the POA value is approximately 0 in the area with flat terrain, while the pixel with a large POA is mainly distributed in the area with a large slope, which is relatively close to the actual ground condition information. From the pixel number percentage of different POA value intervals (Figure 3b), it can be found that the percentage of POA in the ±0.5° interval (approximately flat land) is 50.71%, that is, the proportion of non-flat land is 49.29%, indicating that there is a lot of polarization azimuth deviation. In addition, the percentage of POA distributed in the range of −15° to −45° and 15° to 45° (large deviation angle) is about 1%, indicating that the very large angle POA deviation phenomenon rarely occurs.

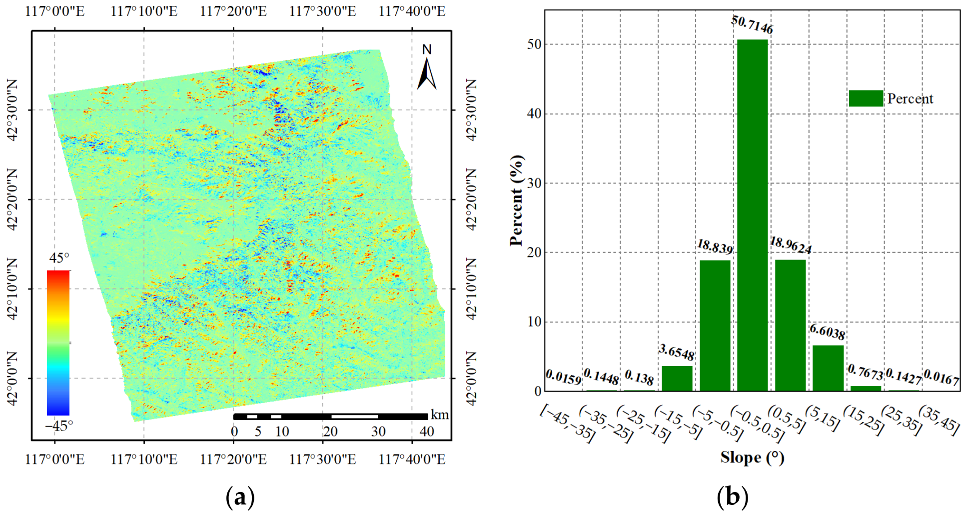

Figure 3. Polarization orientation angle (POA) spatial distribution and numerical distribution: (**a**) Spatial distribution image of POA; (**b**) the percentage of the number of pixels in different POA value intervals.

Figure 4 shows the ESAC factor (Figure 4c) extracted based on Equation (10) with local incidence angle (Figure 4a) and radar incidence angle (Figure 4b) as input parameters. As can be seen from Figure 4d: (1) the ESAC factor value of the pixel at the front slope ($\theta_{loc} < \theta_{ref}$) is less than 1.0, resulting in a decreasing trend of the backscattering coefficient after ESAC; (2) the value of ESAC factor of the pixel on the flat ground ($\theta_{loc} = \theta_{ref}$) is equal to 1.0, resulting in no change in the backscattering coefficient after ESAC, which is equivalent to no ESAC performed on the pixel of flat ground; (3) the ESAC factor value of the pixel at the back slope ($\theta_{loc} > \theta_{ref}$) is greater than 1.0, resulting in an increasing trend of the backscattering coefficient after ESAC; (4) in general, the SAR information of pixels with different slope is similar to that of flat ground under the same conditions by applying ESAC factor.

Figure 5a shows the mask files of the forest cover area extracted by Freeman3 decomposition and Wishart unsupervised classification based on the data after POAC and ESAC. Then, based on the iteration of the cost equation *f(n)* with the lowest correlation coefficient, the point plot of the correlation coefficient between the backscattering coefficient after AVEC and the local incidence angle with different values of ***n*** was obtained (Figure 5b).

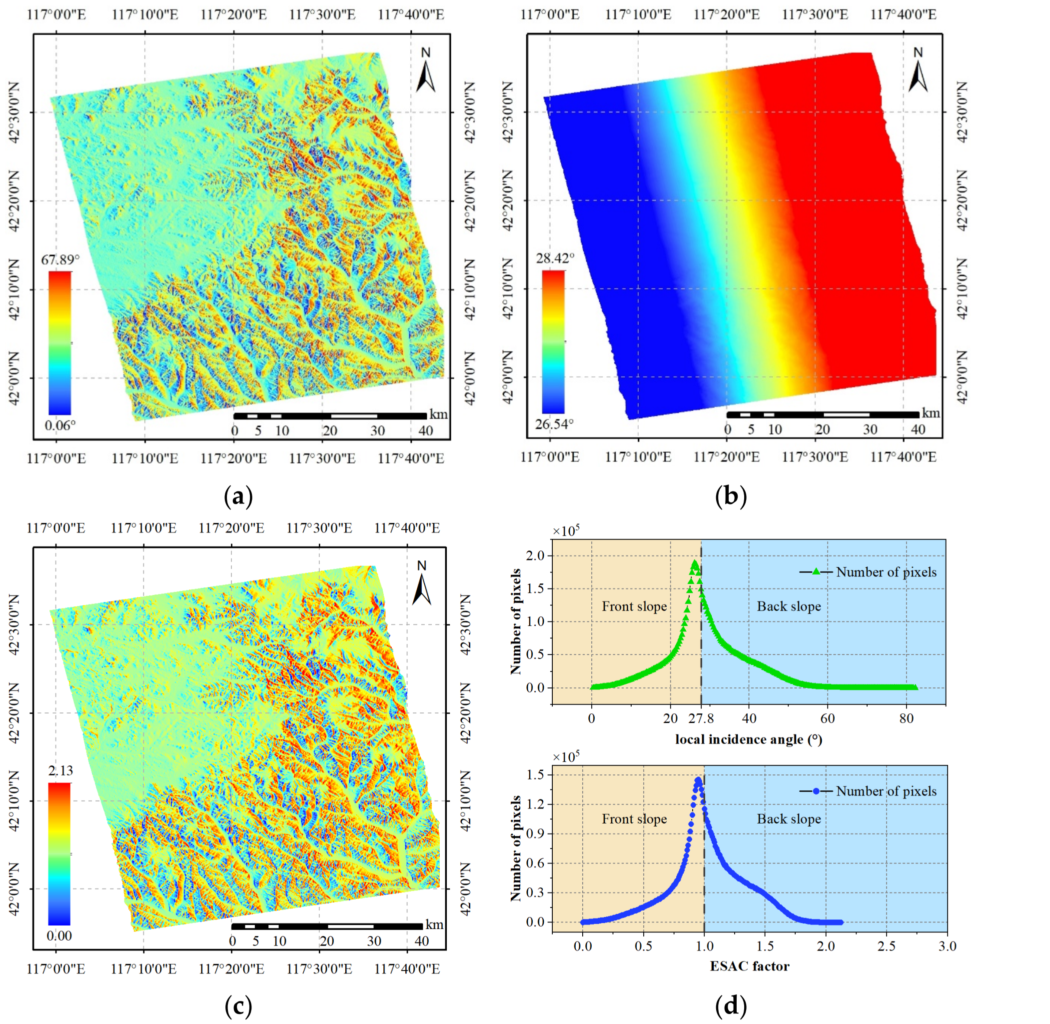

Figure 4. Effective scattering area correction (ESAC) factor: (**a**) Local incidence angle θ_{loc}; (**b**) Radar incidence angle θ_{ref}; (**c**) ESAC factor; (**d**) pixel histogram of local incidence angle and ESAC factor. For the sake of demonstration, (**d**) assumes that the ESAC factor is equal to 1.0 when the local incidence angle is equal to the average radar incidence angle (27.8°).

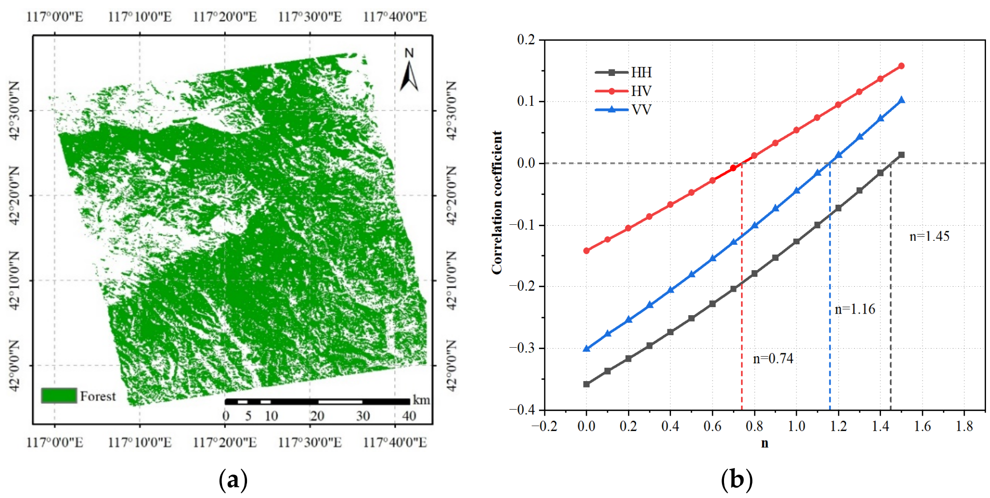

Figure 5. The mask files and the optimal *n* value of angular variation effect correction (AVEC): (**a**) Forest cover mask files extracted based on Freeman3 decomposition and Wishart unsupervised classifier; (**b**) the optimal *n* value of AVEC corresponding to the three polarization channels.

According to the optimal n values of the three polarization channels (Figure 5b), where n_{HV} = 1.45, n_{HV} = 0.74, n_{VV} = 1.16, the final correction coefficient matrix K can be obtained as follows:

$$K = \begin{bmatrix} k(1.45) & k(1.095) & k(1.305) \\ k(1.095) & k(0.74) & k(0.95) \\ k(1.305) & k(0.95) & k(1.16) \end{bmatrix} \quad (18)$$

Table 4 lists the optimal n values corresponding to the three polarization channels of all date data in the PolSAR dataset. Among them, the optimal n values of the three polarization modes of the same date data are different, and the rule of $n_{HV} > n_{HV} > n_{VV}$ exists, indicating that there are different degrees of AVE phenomenon in different SAR data scenes, but among the three polarization channels, the weakest AVE phenomenon exists in the HV polarization channel.

Table 4. The optimal n values for three polarization channels of 5 date data in PolSAR dataset.

	11 July 2020	25 July 2020	8 August 2020	5 September 2020	19 September 2020
HH	1.76	1.45	1.56	1.66	1.82
HV	0.85	0.74	0.72	0.85	1.02
VV	1.45	1.16	1.22	1.34	1.54

4.2. Analyze the Results of Radiometric Terrain Correction

In order to qualitatively analyze the terrain correction effect, Pauli RGB images of NRTC (Figure 6a,e) were used as a blank control. In addition, the Pauli RGB images of each terrain correction stage are compared and displayed, respectively, in the global view (Figure 6a–d) and the local enlarged view (Figure 6e–h). Pauli RGB images (Figure 6b,f) with only POAC completion have no obvious visual changes, and there are still obvious topographic relief phenomena, that is, the front slope is obviously brighter than the back slope. This is because POAC mainly compensates the polarization azimuth deviation caused by azimuth-oriented slope for full-polarization SAR data, and because of the characteristics of SAR side-looking, the visual changes caused by azimuth-oriented slope are less obvious than those caused by range-oriented slope. After further implementation of ESAC, the topographic relief phenomenon of the Pauli RGB image (Figure 6c,g) has been significantly improved, but a slight topographic relief phenomenon can still be seen in some areas such as ridges, indicating that the radiation distortion caused by terrain has been greatly reduced, but the influence of terrain cannot be completely removed. After the completion of AVEC, Pauli RGB images (Figure 6d,h) almost did not have topographic relief, indicating that AVEC further eliminated topographic effects on the basis of ESAC.

In order to evaluate the effectiveness of the three-step correction method, the relationship between POA and the difference of the backscattering coefficients (σHV before POAC minus σHV after POAC) of the three polarization channels before and after POAC was first quantitatively analyzed (Figure 7). Among them, the value ranges of Δ_σHH (Figure 7a), Δ_σHV (Figure 7b) and Δ_σVV (Figure 7c) all increase with the increase in POA, indicating that the degree of correction is positively correlated with the size of POA. The values of Δ_σHH and Δ_σVV are both positive and negative, but the values of Δ_σHV are both positive, indicating that POA migration will lead to the overestimation of the σ^0 of HV polarization, while the σ^0 of HH and VV polarization has no obvious overestimation or underestimation law. Δ_σHH has more positive values and is distributed in the interval of (−0.5, 1.5) dB, while Δ_σVV has more negative values and is distributed in the interval of (−2.0, 0.5) dB, indicating that POAC has different degrees of correction for the three polarization channels. According to the scatter density diagram of Δ_σHH and Δ_σVV (Figure 7d), it can be found that the two are roughly negatively correlated, and they cannot be positive at the same time because Δ_σHV are both positive, indicating that POAC meets the law of conservation of energy and only re-adjusts the scattering information of different polarization modes without increasing or reducing the total scattering power.

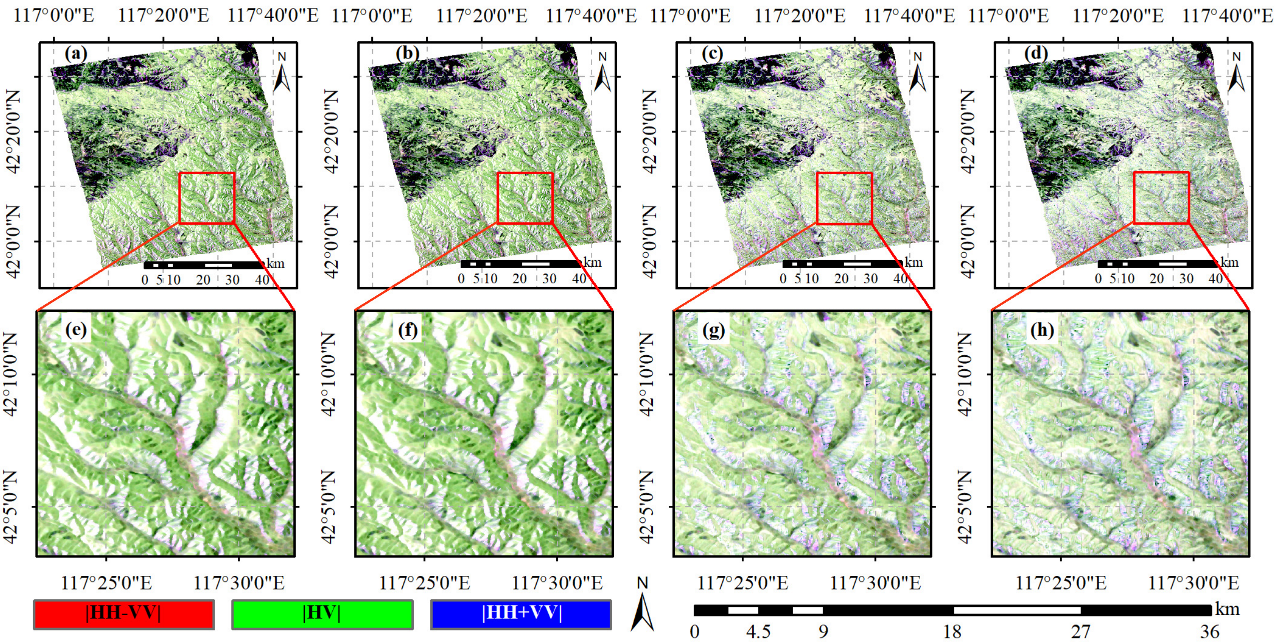

Figure 6. Pauli RGB images of different radiometric terrain correction (RTC) stages in global view and local view: (**a**) Global view after no radiometric terrain correction (NRTC); (**b**) global view after polarization orientation angle correction (POAC); (**c**) global view after effective scattering area correction (ESAC); (**d**) global view after angular variation effect correction (AVEC); (**e**) local view after NRTC; (**f**) local view after POAC; (**g**) local view after ESAC; (**h**) local view after AVEC.

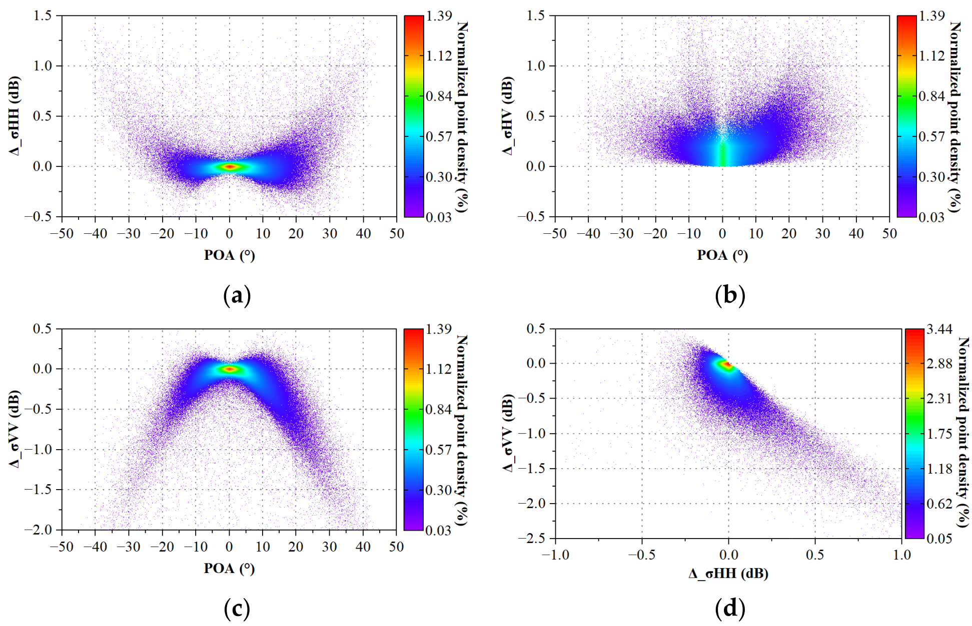

Figure 7. Scatter density plots of the difference between PolSAR data before and after polarization orientation angle correction (POAC) and the polarization orientation angle (POA): (**a**) Δ_σHH vs. POA; (**b**) Δ_σHV vs. POA; (**c**) Δ_σVV vs. POA; (**d**) Δ_σHH vs. Δ_σVV.

Subsequently, the relationship between σ^0 of different polarization channels and θ_{loc} at different RTC stages was analyzed (Figure 8). In the NRTC stage (Figure 8a–c), there is an obvious linear relationship between the backscattering coefficient of each polarization channel and θ_{loc}. This linear relationship is still evident in the data after POAC (Figure 8d–f), because the effect of POAC is to eliminate the effect of POA rather than the effect of θ_{loc}. However, this linear relationship is greatly weakened in the data after ESAC (Figure 8g–i), indicating that

ESAC correction plays a great role in removing the influence of local incidence angle. Finally, in the data after AVEC (Figure 8j–l), this linear relationship almost disappears, indicating that AVEC also plays a role.

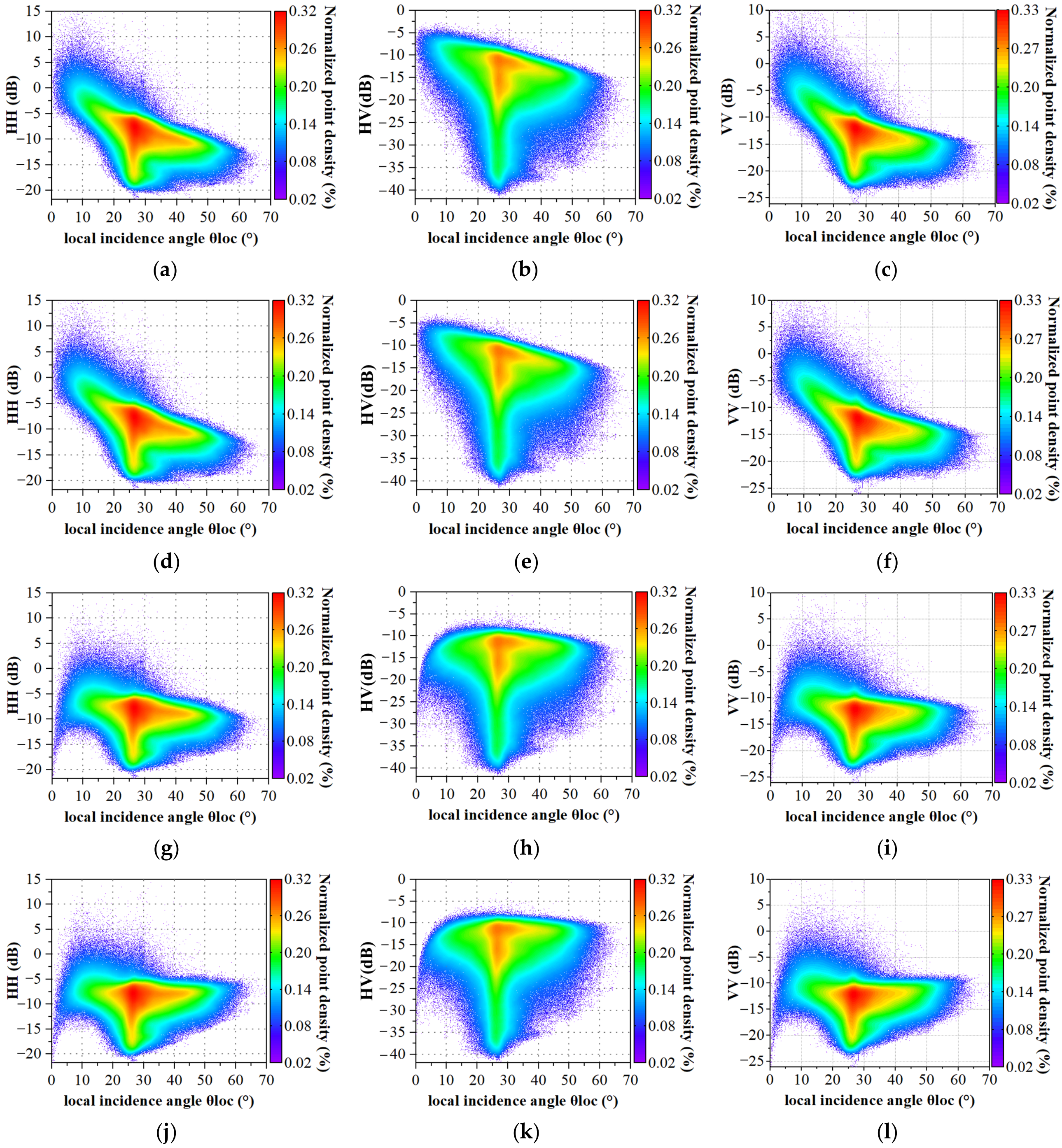

Figure 8. Scatter density plots of local incidence angles θ_{loc} and backscattering coefficients at different correction stages, including no radiometric terrain correction (NRTC), polarization orientation angle correction (POAC), effective scattering area correction (ESAC) and angular variation effect correction (AVEC). (**a**) HH$_{_NRTC}$; (**b**) HV$_{_NRTC}$; (**c**) VV$_{_NRTC}$; (**d**) HH$_{_POAC}$; (**e**) HV$_{_POAC}$; (**f**) VV$_{_POAC}$; (**g**) HH$_{_ESAC}$; (**h**) HV$_{_ESAC}$; (**i**) VV$_{_ESAC}$; (**j**) HH$_{_AVEC}$; (**k**) HV$_{_AVEC}$; (**l**) VV$_{_AVEC}$.

4.3. Correlation Analysis between Radiometric Terrain Correction and AGB

In order to analyze the effects of different RTC stages on AGB inversion, the correlation between the measured AGB and the backscattering of the three polarization channels was analyzed using the data dated 25 July 2020 as an example. It can be seen from Table 5 that among the three polarization channels in the same RTC stage, the correlation coefficient (R) of the HV polarization channel has the largest value. With the advance of the RTC stage, the R values of the three polarization channels are steadily increasing, and compared with the data of the NRTC, the HH, HV, and VV polarization channels have increased by 0.399, 0.310, and 0.404, respectively. The ESAC stage has the most obvious improvement on R, and the three polarization channels are 0.343, 0.296, and 0.382, respectively. Taking the HV polarization channel as an example, POAC, ESAC, and AVEC increase the R value by 0.002, 0.296, and 0.012, respectively. The contribution of POAC is the least, which indicates that POAC has limited ability to correct this area. The ESAC plays a major role in effectively weakening the effect of terrain, which indicates the rationality and effectiveness of the ESAC method with the introduction of normalized correction factors. In the AVEC stage, the terrain correction effect of the same polarization is better than that of the HV polarization, because the optimal n value of the same polarization is greater than that of the HV, and the size of the optimal n value is proportional to the correction force. However, the contribution of AVEC is relatively insignificant, but from the side, it shows that ESAC is more thorough.

Table 5. The correlation coefficient (R) between the measured AGB (dB) and the backscattering coefficients of the three polarization channels of PolSAR data (dated 25 July 2020) at different RTC stages.

	NRTC	**POAC**	**ESAC**	**AVEC**
HH	0.306	0.307	0.650	0.705
HV	0.542	0.544	0.840	0.852
VV	0.336	0.338	0.720	0.740

4.4. Robustness Analysis of Radiometric Terrain Correction

To explore the robustness of the RTC under various AGB inversion models and PolSAR data, we first fit five AGB inversion models (Equation (14)) at each stage of the RTC and evaluate these models. It can be seen from Table 6 that in all the tested models, R^2 values of the three polarization channels increase with the advance of the RTC stage, indicating that different RTC stages can play a role in these five models, and the contribution of ESAC is the most obvious. In addition, among the three polarization channels, the R^2 value of the HV polarization channel is the largest, indicating that the backscattering coefficient of the HV polarization mode has the best fitting effect with AGB. Compared with M0, M1 has better fitting results at any RTC stage, indicating that AGB is not simply linear with the backscattering coefficient and that the logarithmic transformation of AGB can effectively improve its fitting effect with the backscattering coefficient. Although model 3 (M3) is numerically optimal, there is no quadratic polynomial relationship between AGB and backscattering coefficient in theory, which indicates that the model is overfitting. However, the R^2 value of M3 steadily increases in each stage of RTC, indicating that the terrain correction effect of the RTC process is still relatively robust for M3. Although model 4 (M4) has a better R^2 value without RTC, it has a greater improvement after RTC, indicating that the backscattering coefficients of HH and VV polarization channels can also contribute to AGB estimation. Compared with the independent use of HV polarization channel (M2), the simultaneous participation of three polarization channels in AGB inversion can compensate for the influence of terrain and has better AGB inversion potential, but RTC is still essential. In conclusion, RTC has good robustness in different statistical models, among which M2 is the best univariate model, and the backscattering coefficient of the HV polarization channel has the best fitting effect with the measured AGB, which can be used as the best variable of the univariate model. In addition, M4 is slightly better than M2, which has greater inversion potential.

Table 6. R^2 values under different inversion models: Taking the data dated 25 July 2020 as an example, the R^2 of the measured AGB and the backscattering coefficients of the three polarization channels (HH/HV/VV) under different inversion modes and different RTC stages are listed.

	NRTC	**POAC**	**ESAC**	**AVEC**
M0	0.033/0.151/0.060	0.033/0.153/0.060	0.261/0.442/0.401	0.396/0.490/0.510
M1	0.05/0.198/0.08	0.05/0.201/0.08	0.336/0.510/0.463	0.447/0.554/0.531
M2	0.094/0.293/0.113	0.123/0.296/0.115	0.423/0.705/0.518	0.497/0.726/0.548
M3	0.365/0.621/0.421	0.366/0.622/0.423	0.635/0.772/0.696	0.619/0.794/0.675
M4	0.609	0.619	0.719	0.730

Second, we analyzed the robustness of the RTC process in PolSAR data based on the most widely used M2 model and the backscattering coefficients of the HV polarization channels with data from 5 dates. It can be seen from Table 7 that the data of different dates have roughly the same rule, that is, the fitting results of different RTC stages are gradually improved with the implementation of RTC stages. In particular, the improvement of the R^2 value in the ESAC stage (0.397, 0.409, 0.422, 0.430, and 0.381) is extremely significant and stable. In the data of 5 dates, the RTC process increased R^2 by 0.405, 0.433, 0.421, 0.431, and 0.395, respectively. However, in the data dated 8 August 2020, the value of R^2 in the AVEC phase is slightly smaller than that in the ESAC phase, and in the data dated 5 September 2020, the value of R^2 in the POAC phase is slightly smaller than that in the NRTC phase. These results indicate that RTC is robust in PolSAR data, with an average increase of 0.417 in R^2, especially in the ESAC phase, with an average increase of 0.408 in R^2, but there may be exceptions in POAC and AVEC.

Table 7. The R^2 value of the most stable model M2: Lists the R^2 value of the measured AGB and the backscattering coefficient of the HV polarization channel in the data of 5 dates at different stages of RTC based on M2.

	11 July 2020	**25 July 2020**	**8 August 2020**	**5 September 2020**	**19 September 2020**
NRTC	0.232	0.293	0.266	0.289	0.271
POAC	0.234	0.296	0.267	0.289	0.274
ESAC	0.631	0.705	0.689	0.719	0.655
AVEC	0.637	0.726	0.687	0.720	0.666

It can be seen from the scatter plot of the validation set of measured data and the predicted data (Figure 9) that regression models with different date data have good generalization ability and are sufficient to predict the AGB of the study area.

Finally, based on the data of 5 dates and the fitted regression equation, the corresponding AGB is inverted, respectively, and the average value of the data of 5 periods is taken as the final AGB result (Figure 10).

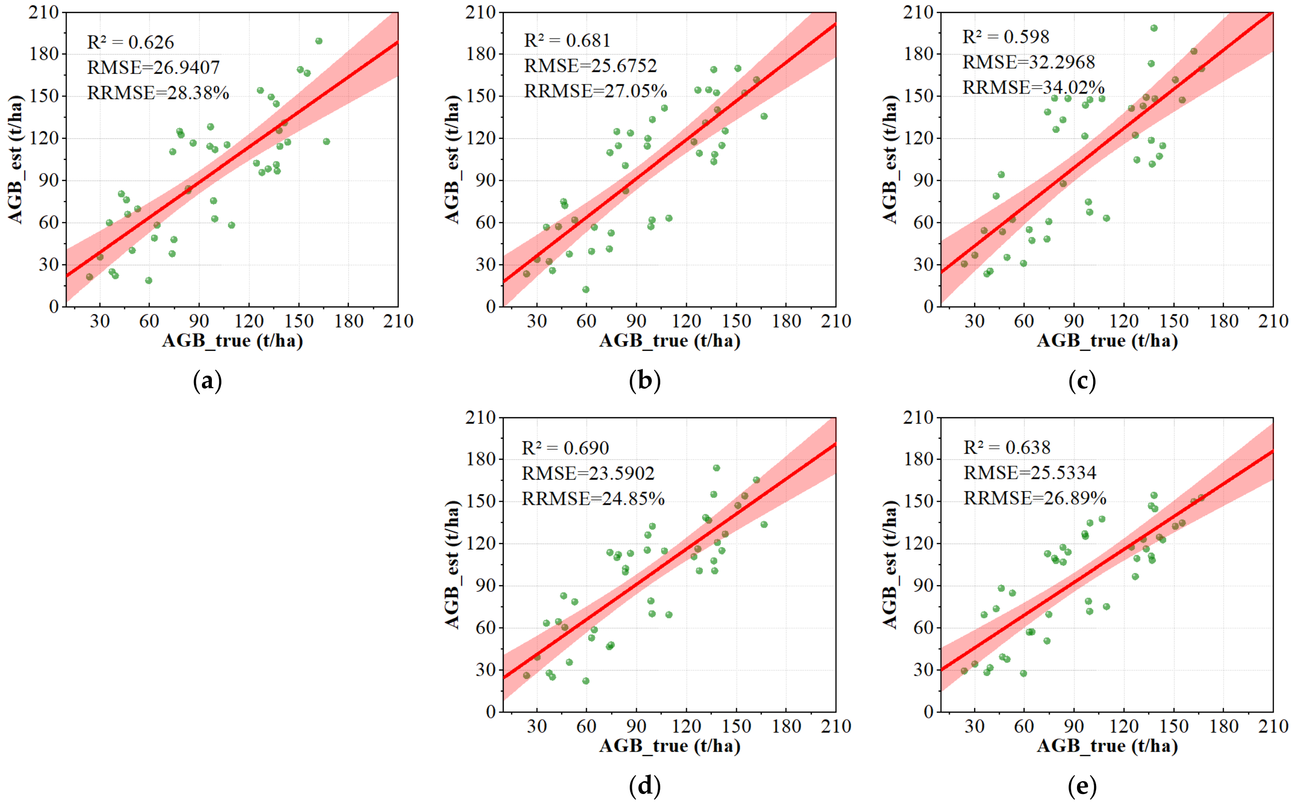

Figure 9. Scatter plot of measured AGB and AGB predicted by PolSAR data at different dates, where the olive dots are the sample plots, the red lines are the fit lines, and the red (70% transparency) filled areas are 95% confidence intervals: (**a**) 11 July 2020; (**b**) 25 July 2020; (**c**) 8 August 2020; (**d**) 5 September 2020; (**e**) 19 September 2020.

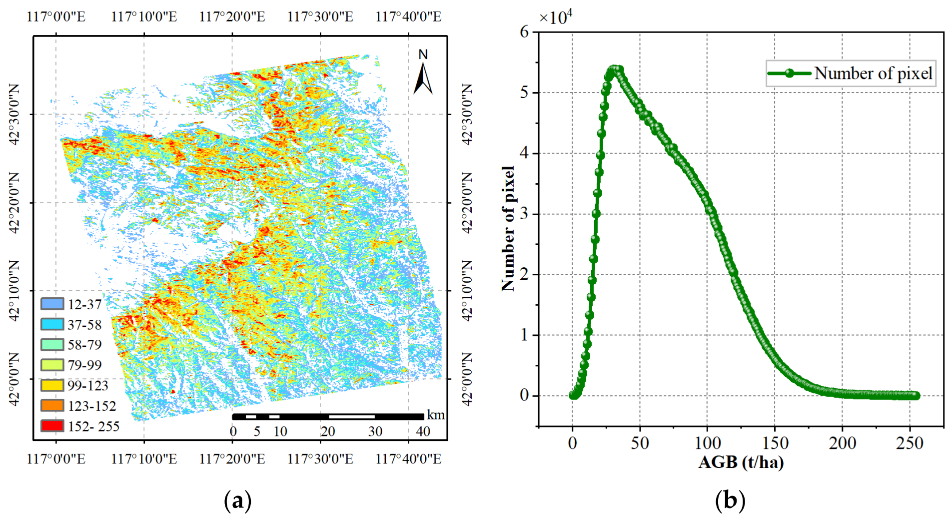

Figure 10. AGB estimation results of Saihanba research area based on the average data of 5 phases: (**a**) AGB spatial distribution; (**b**) AGB histogram.

5. Discussion

In this study, a normalized correction factor was introduced in the ESAC stage of RTC. This correction factor is based on the local incidence angle and radar incidence angle to fine-adjust ground units of different slopes, effectively reducing the influence of terrain on the backscattering coefficient of SAR data, and greatly improving the accuracy of AGB inversion based on the backscattering coefficient.

5.1. The Application Potential of Radiometric Terrain Correction

Accurate inversion of forest AGB can more accurately estimate the carbon budget at regional and even global scales, which is of great significance for understanding and predicting the trend of global climate change and formulating coping strategies. However, our results show that the existence of topographic factors has a great influence on the accurate inversion of forest AGB. Taking the PolSAR data of 25 July 2020 as an example, the correlation coefficient R values of the backscattering coefficients after the three polarized channels after RTC and the measured AGB increased by 0.399, 0.310, and 0.404 respectively, indicating that the existence of topographic factors introduced many interference terms, which leads to a sharp decline in the sensitivity of PolSAR characteristic parameters and AGB. In addition, although RTC has different performance in different forest AGB models, the model results based on the backscattering coefficient fitting after RTC are improved to different degrees. Take M2 as an example; its R^2 value is increased by 0.403, 0.433, and 0.435, indicating that the accuracy of AGB extracted without the RTC process is worrying and that it is almost impossible to apply. However, AGB based on backscatter coefficient inversion after RTC greatly improves the accuracy of AGB inversion. It can be seen that RTC is of great significance to the precise mapping and application of AGB in mountainous forest areas with complex terrain. Moreover, understanding AGB trends in specific regions or ecosystems can help decision makers assess the status of forest resources, formulate reasonable forest management and restoration measures, and maintain and improve the stability and service functions of ecosystems.

In mountainous forest areas with complex terrain, AGB inversion based on a non-parametric model and different forestry applications based on SAR technology (InSAR, PolInSAR, TomoSAR) (forest canopy height extraction, forest type classification), if the impact of terrain is considered, analysis and establishment of a suitable RTC process to remove the interference of terrain factors can improve the inversion effect to a certain extent.

5.2. The Effectiveness of Radiometric Terrain Correction

This study uses the RTC process, including POAC, ESAC, and AVEC, and the results of previous studies are similar [43,64]: RTC has a large increase in the correlation between backscattering coefficient and AGB, in which ESAC is the most important, while POAC and AVEC contribute less.

In the POAC stage, the backscattering information of different polarization channels is compensated for by the polarization azimuth shift, but the effect on the change of vision and the enhancement of the correlation between σ^0 and AGB is not obvious. The reason for the lack of visual change is that POAC in theory mainly compensates for the deviation of the polarization azimuth caused by the azimuth slope. Due to the side view of SAR, the correction of the azimuth angle cannot be displayed well in the visual view. In addition, POAC mainly corrects the change in polarization state caused by terrain and may have a more obvious influence on the information, such as polarization decomposition [74]. The reason why POAC's effect on improving the correlation between σ^0 and AGB is not obvious is that POA is not only affected by terrain, but also by forest canopy. In the case that POA caused by forest canopy and POA caused by terrain are not separated, POAC has a correction problem, and new errors are introduced during correction. As a result, POAC does not play its best role. Therefore, how to separate the POA offset caused by the canopy from the POA offset caused by the topography under the canopy is still a problem to be solved.

In the ESAC stage, aiming at the backscattering coefficient and C3 matrix, this study introduced a normalized correction factor based on the local incidence angle and radar incidence angle, and its value distribution was (0, 2.13]. When the local incidence angle was equal to the radar incidence angle, the ground unit belonged to flat ground and did not need to be corrected, so the corresponding correction factor was equal to 1.0. When the local incidence angle is less than the radar incidence angle, the ground unit belongs to the front slope. Compared with flat ground, the existence of terrain leads to the enhancement of backscatter. Therefore, the correction factor range is (0, 1.0) for the front slope, and the opposite is true for the local incidence angle less than the radar incidence angle. The existing studies [43,64] are all based on the projection angle or local incidence angle, and the value is distributed between (0, 1.0], which only converts the ground backscattering coefficient to the isophase backscattering coefficient γ^0. However, if the equation is directly applied to the C3 matrix without modification, the C3 matrix corresponding to the flat ground, which should not be corrected, will be modified. Consistent with their study, ESAC showed a large improvement in the correlation of both σ^0 and AGB, and provided the largest correction contribution in the overall topographic radiometric correction. In addition, previous studies [55] have shown that the area integration method under the slan-distance geometry of SAR, which is more in line with the SAR imaging mechanism, can improve the ESAC effect. However, since the resolution of DEM data is much lower than that of the original PolSAR data, the accurate estimation of the ground unit area corresponding to the oblique azimuth pixel is seriously limited, so the research can be done after the high-precision digital terrain model (DTM) is available.

In the AVEC stage, terrain correction has different correction effects on different polarization channels, among which HH > VV > HV, which is not only reflected in the numerical rule of the optimal n value (Table 4), but also in the correlation between σ^0 and AGB of the three polarized channels in the AVEC stage. For example, the three polarized channels in the AVEC stage increased by 0.055, 0.012, and 0.020, respectively (Table 5). However, there is no obvious rule for the optimal n value of different scene data because AVEC is highly correlated with the terrain coverage type in the study area. In addition, it also indicates that the extraction method of adaptive determination of the optimal n value is highly practical. The reason why the AVEC stage is not effective in improving the correlation between σ^0 and AGB is that the backscattering coefficient is related to multiple factors such as complex dielectric constant, terrain slope, surface roughness, etc., while AVEC only considers the local incidence angle and radar incidence angle, resulting in the unsatisfactory correction of the scattering mechanism. How to consider more influencing factors in the AVEC basic model and determine these values adaptively is a problem worth studying. In addition, AVEC is mainly to correct the effect of terrain on the scattering mechanism, so it is difficult to show the correction effect in the backward scattering coefficient, which is another reason. To demonstrate the effect of AVEC on the polarization decomposition is the next research goal.

5.3. The Robustness of Radiometric Terrain Correction

This study demonstrates that RTC is robust to different models and different data, especially in the ESAC phase, based on the introduced normalized correction factor. This is because, compared with the statistical modeling method that integrates terrain factors in AGB modeling, RTC is based on the SAR imaging mechanism and scattering mechanism. Each stage of RTC has specific and clear physical significance, and it is a targeted correction for the radiation distortion caused by terrain, so it has good robustness.

We used five models to verify the robustness of RTC in different models. However, we only tested five common models, while most other models were not tested, and the comparison between different models was not comprehensive enough. For example, compared with the univariate model in which HV polarized channels participate, the fitting of the multivariate linear model in which three polarized channels participate at the same time helps to improve the value of R^2, and most studies [64,75] have reached similar conclusions. However, in fact, the R^2 values of the multivariate model and the monadic model are not very different. Moreover, multivariate models often need to consider collinearity, and when multivariate models contain variables used by monadic models and add multiple independent variables, the R^2 value of multivariate models is bound to increase. Therefore, whether the multivariate model is much better than the monadic model needs to be further demonstrated, but the multivariate model has greater application potential.

In addition, PolSAR data of different dates are not fully applicable in the POAC and AVEC stages of RTC (Table 7), because the weather conditions at the time of satellite data collection will also bring certain errors to the accurate inversion of AGB. Furthermore, we only validated ALOS2 data for five dates, but did not test other PolSAR data products, so it is not comprehensive enough to validate robustness on different types of data.

5.4. Potential Other Limitations

Parameters such as local incidence angle and projection angle required for the RTC process based on PolSAR data are extremely related to DEM data. However, the existing DEM data are digital surface model (DSM) rather than DTM, and the resolution of the existing DEM is too low (30 m) to provide accurate terrain slope information. There are some errors in the local incidence angle and projection angle, which limit the effect of RTC. PolInSAR technology has the ability to extract high-precision and high-resolution DTM data, which is expected to solve the limitations of DEM.

In this study, due to the limitation of manpower, we could not set up sample plots in forest areas with steep terrain. Therefore, there were no measured sample plots with large slopes in our test area, resulting in a lack of samples of extreme terrain, and the analysis of different grades of slope was not carried out. The unmanned aerial vehicle-light detecting and ranging (UAV-LiDAR) system is capable of collecting sample data with high precision and is expected to acquire forest parameter information for forest regions with more extreme terrain, providing more comprehensive verification samples.

In addition, for regions with complex forest structure (non-uniform), operations using neighborhood averaging (such as multilooking and polarimetric speckle filtering) will result in mixed averaging of forest and non-forest pixels, resulting in large error of target pixels, and also affect the accurate inversion of AGB. Solving the mixed average problem of different types of pixels is the future research direction.

For the choice of parametric model and non-parametric model, this study aims to introduce normalized terrain correction factors into the ESAC stage of RTC and explore the effectiveness and robustness of the RTC process, so a more widely used and more explanatory parameter model is adopted. However, if the actual data distribution is inconsistent with the model hypothesis, the parameter model may be biased. In addition, in the face of complex nonlinear relationships and high-dimensional variables in the dataset, the parameter model may oversimplify the data structure and lead to the problem of underfitting or overfitting. However, the non-parametric model can adapt to complex data with different structures without presupposing the specific form of the model, so it has good flexibility and robustness and is especially suitable for processing high-dimensional data. Therefore, exploring non-parametric models such as machine learning algorithms based on RTC-corrected data is expected to further improve the inversion accuracy of AGB.

6. Conclusions

In order to make better use of PolSAR data to accurately estimate the AGB of the terrain of a complex region, the disturbance caused by terrain becomes a problem that must be solved. This study combined the RTC process, introduced a normalized correction factor in the ESAC stage, and verified the effectiveness and robustness of the method theoretically and empirically through experiments on ALOS-2 PolSAR data. Here is a summary of the findings: Applying the RTC process of the normalized correction factor in the ESAC stage has good effectiveness in improving the AGB inversion based on the backscattering coefficient and has good robustness in different inversion models and PolSAR data of different dates. Among them, the RTC process can effectively reduce the influence of terrain, which not only greatly changes the visual image but also greatly improves the correlation between the backscattering coefficient and AGB. The POAC, ESAC, and AVEC stages of RTC all have certain contributions, especially the contribution of ESAC, which is much greater than that of POAC and AVEC. In addition, the backscattering coefficients of different polarized channels do not have a simple linear relationship with AGB in linear units but have a good linear relationship with AGB after logarithmic transformation. Moreover, among the three polarization channels, the backscattering coefficient of the HV polarization channel has the highest correlation with AGB. The multivariable model has greater potential to invert AGB than the univariate model.

In addition, the restrictive factors of DEM still exist, and PolInSAR technology is expected to improve the topographic radiation correction effect by extracting the challenges related to high-precision DTM inversion and thus enhance the application of PolSAR data such as AGB inversion.

To sum up, this study deeply studied the impact of topographic factors on the inversion of forest AGB based on the backscattering coefficient of PolSAR data, which helps us better understand the mechanism and process of terrain's impact on PolSAR data, and also introduced the normalized ESAC factor, which is conducive to more accurate terrain correction of SAR data. Moreover, it is verified that RTC can effectively and robustly eliminate the influence of terrain, improve the accuracy of AGB inversion in mountainous forest areas greatly affected by terrain, balance the operability of the technical model and the practicality of AGB inversion in mountainous forest areas, and provide an effective case for the application of PolSAR data in complex terrain areas.

Author Contributions: Conceptualization, Y.N. and W.F.; methodology, Y.N.; software, Y.N.; validation, Y.N.; formal analysis, Y.N.; investigation, Y.N. and W.F.; resources, W.F.; data curation, Y.N. and R.S.; writing—original draft preparation, Y.N.; writing—review and editing, Y.N.; visualization, Y.N. and Y.H.; project administration, Y.N. and W.F.; funding acquisition, W.F. All authors have read and agreed to the published version of the manuscript.

Funding: This research was funded by the National Natural Science Foundation of China (contract no. 31971654) and the Civil Aerospace Technology Advance Research Project (contract no. D040114).

Data Availability Statement: The data presented in this study are available on request from the corresponding author. The data are not publicly available due to privacy.

Acknowledgments: Thanks to JAXA for providing ALOS-2 PALSAR-2 PolSAR data (contract no. AL-DQ-200521-01). Thanks to the Sentinel Application Platform (SNAP_v9.0.0) and Polarimetric SAR Data Processing and Educational Toolbox (PolSARpro_v5.1.1) software developed by ESA. The authors express their sincere thanks and appreciation to the reviewers whose comments and expert advice were instrumental in shaping the contents of this paper.

Conflicts of Interest: The authors declare no conflicts of interest.

Appendix A

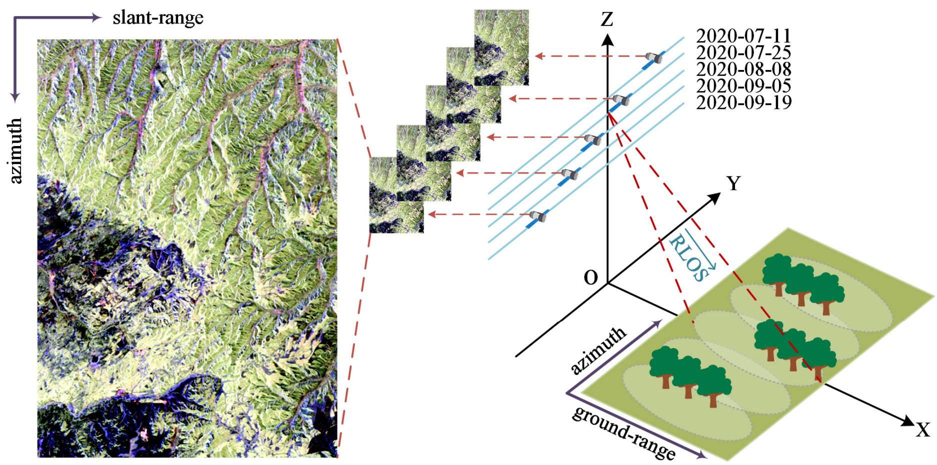

Figure A1. Polarimetric SAR dataset schematic diagram. The big picture on the left is Pauli RGB image of polarization coherency matrix (T3) after 4 × 9 (range × azimuth) multi-look processing on

19 September 2020. The five small pictures in the middle are reduced view of the Pauli RGB image T3 after 4 × 9 (range × azimuth) multi-look processing of data from 5 dates. The picture on the right is SAR imaging geometry in strip mode.

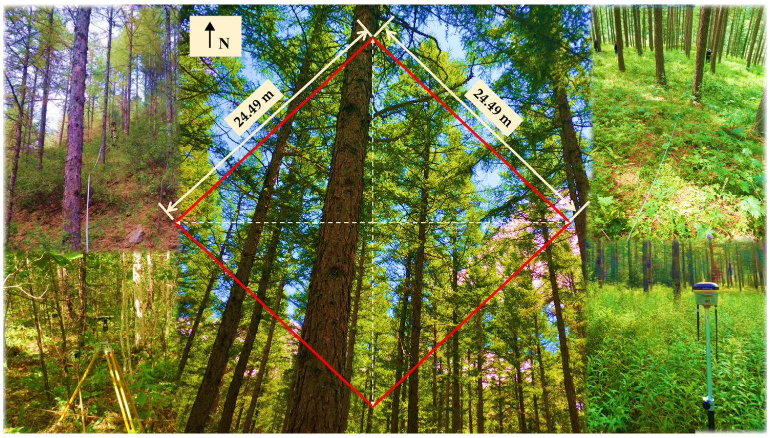

Figure A2. Plot layout and data measurement.

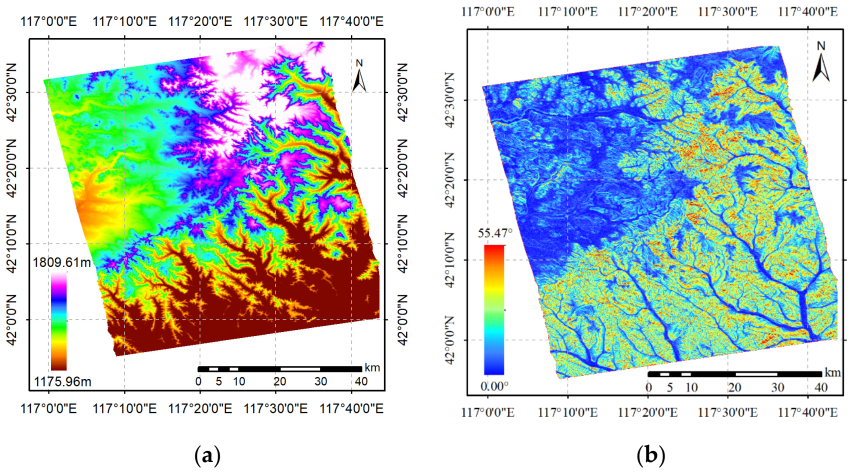

Figure A3. SRTM DEM data: (**a**) SRTM DEM; (**b**) slope map extracted based on DEM.

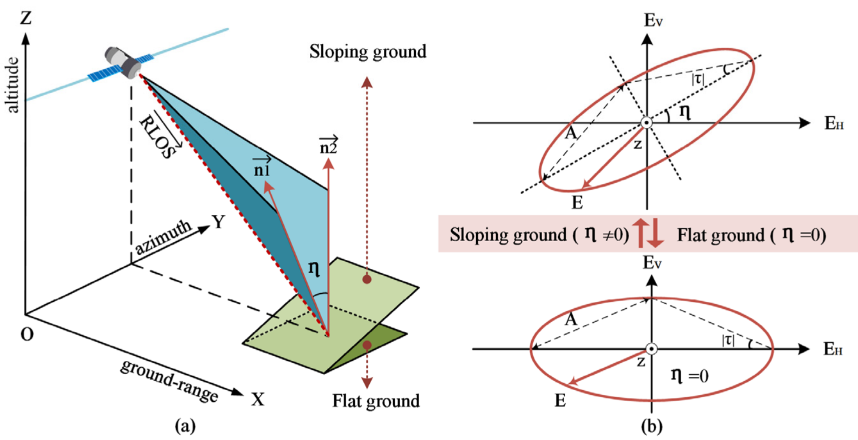

Figure A4. 3D and 2D schematic of polarization azimuth deviation: (**a**) The rotation diagram of the imaging surface normal vector around the radar line of sight (RLOS) in the case of slope vs. flat land in 3D geometric perspective. Among them, $n1$ and $n2$ are normal vectors of slope and land respectively, η with rotation angle, equivalent to polarization orientation angle (POA); (**b**) polarization ellipses of flat and sloping land from a 2D geometric perspective. Where E is the actual electric field vector, E_H is the horizontal component direction, E_V is the vertical component direction, η is the polarization direction angle, τ is the ellipticity angle. The red up and down arrow represent the transformation of the polarization ellipse between the flat and the sloping ground under different values of η, and represent the position direction of the polarization ellipse diagram under the corresponding conditions.

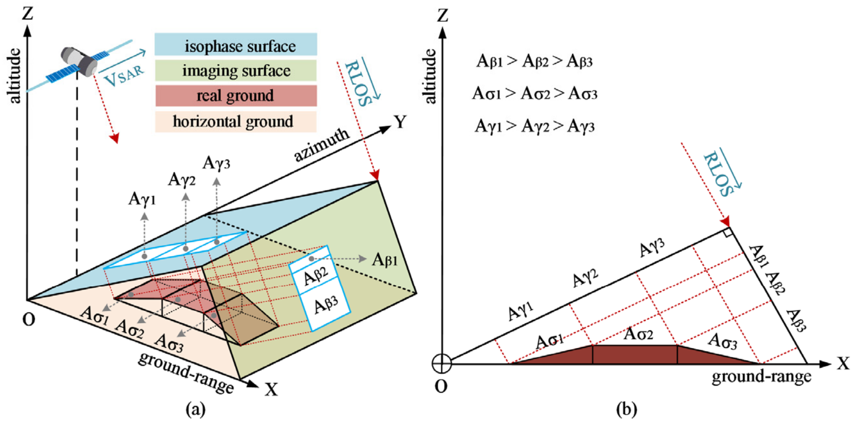

Figure A5. 3D and 2D schematic of the effective scattering area (ESA) corresponding to horizontal ground units with the same area but different slope: (**a**) 3D; (**b**) 2D.

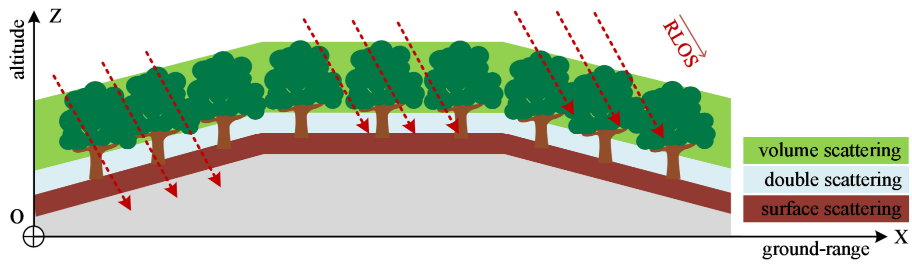

Figure A6. Effect of angular variation effect (AVE) on scattering mechanism. The dotted red arrow represents the radar line of sight (RLOS).

References

1. Falkowski, P.; Scholes, R.J.; Boyle, E.; Canadell, J.; Canfield, D.; Elser, J.; Gruber, N.; Hibbard, K.; Högberg, P.; Linder, S.; et al. The Global Carbon Cycle: A Test of Our Knowledge of Earth as a System. *Science* **2000**, *290*, 291–296. [CrossRef]
2. Pan, Y.; Birdsey, R.A.; Fang, J.; Houghton, R.; Kauppi, P.E.; Kurz, W.A.; Phillips, O.L.; Shvidenko, A.; Lewis, S.L.; Canadell, J.G.; et al. A Large and Persistent Carbon Sink in the World's Forests. *Science* **2011**, *333*, 988–993. [CrossRef]
3. Xiao, J.; Chevallier, F.; Gomez, C.; Guanter, L.; Hicke, J.A.; Huete, A.R.; Ichii, K.; Ni, W.; Pang, Y.; Rahman, A.F.; et al. Remote Sensing of the Terrestrial Carbon Cycle: A Review of Advances over 50 Years. *Remote Sens. Environ.* **2019**, *233*, 111383. [CrossRef]
4. Sugden, A.; Smith, J.; Pennisi, E. The Future of Forests. *Science* **2008**, *320*, 1435. [CrossRef] [PubMed]
5. Houghton, R.A.; Hall, F.; Goetz, S.J. Importance of Biomass in the Global Carbon Cycle. *J. Geophys. Res. Biogeosci.* **2009**, *114*, JG000935. [CrossRef]
6. Vashum, K.T. Methods to Estimate Above-Ground Biomass and Carbon Stock in Natural Forests—A Review. *J. Ecosyst. Ecogr.* **2012**, *2*, 1000116. [CrossRef]
7. Moreira, A.; Prats-Iraola, P.; Younis, M.; Krieger, G.; Hajnsek, I.; Papathanassiou, K.P. A Tutorial on Synthetic Aperture Radar. *IEEE Geosci. Remote Sens. Mag.* **2013**, *1*, 6–43. [CrossRef]
8. Tsokas, A.; Rysz, M.; Pardalos, P.M.; Dipple, K. SAR Data Applications in Earth Observation: An Overview. *Expert Syst. Appl.* **2022**, *205*, 117342. [CrossRef]
9. Sinha, S.; Jeganathan, C.; Sharma, L.K.; Nathawat, M.S. A Review of Radar Remote Sensing for Biomass Estimation. *Int. J. Environ. Sci. Technol.* **2015**, *12*, 1779–1792. [CrossRef]
10. Lu, D.; Chen, Q.; Wang, G.; Liu, L.; Li, G.; Moran, E. A Survey of Remote Sensing-Based Aboveground Biomass Estimation Methods in Forest Ecosystems. *Int. J. Digit. Earth* **2016**, *9*, 63–105. [CrossRef]

11. Steininger, M.K. Satellite Estimation of Tropical Secondary Forest Above-Ground Biomass: Data from Brazil and Bolivia. *Int. J. Remote Sens.* **2000**, *21*, 1139–1157. [CrossRef]
12. Lu, D.; Chen, Q.; Wang, G.; Moran, E.; Batistella, M.; Zhang, M.; Vaglio Laurin, G.; Saah, D. Aboveground Forest Biomass Estimation with Landsat and LiDAR Data and Uncertainty Analysis of the Estimates. *Int. J. For. Res.* **2012**, *2012*, 436537. [CrossRef]
13. Zhu, X.; Liu, D. Improving Forest Aboveground Biomass Estimation Using Seasonal Landsat NDVI Time-Series. *ISPRS J. Photogramm. Remote Sens.* **2015**, *102*, 222–231. [CrossRef]
14. Tian, L.; Wu, X.; Tao, Y.; Li, M.; Qian, C.; Liao, L.; Fu, W. Review of Remote Sensing-Based Methods for Forest Aboveground Biomass Estimation: Progress, Challenges, and Prospects. *Forests* **2023**, *14*, 1086. [CrossRef]
15. Borlaf-Mena, I.; Santoro, M.; Villard, L.; Badea, O.; Tanase, M. Investigating the Impact of Digital Elevation Models on Sentinel-1 Backscatter and Coherence Observations. *Remote Sens.* **2020**, *12*, 3016. [CrossRef]
16. Le Toan, T.; Beaudoin, A.; Riom, J.; Guyon, D. Relating Forest Biomass to SAR Data. *IEEE Trans. Geosci. Remote Sens.* **1992**, *30*, 403–411. [CrossRef]
17. Mitchard, E.T.A.; Saatchi, S.S.; Woodhouse, I.H.; Nangendo, G.; Ribeiro, N.S.; Williams, M.; Ryan, C.M.; Lewis, S.L.; Feldpausch, T.R.; Meir, P. Using Satellite Radar Backscatter to Predict Above-ground Woody Biomass: A Consistent Relationship across Four Different African Landscapes. *Geophys. Res. Lett.* **2009**, *36*, GL040692. [CrossRef]
18. Li, W.; Chen, E.; Li, Z.; Zhang, W.; Jiang, C. Assessing Performance of Tomo-SAR and Backscattering Coefficient for Hemi-Boreal Forest Aboveground Biomass Estimation. *J. Indian Soc. Remote Sens.* **2016**, *44*, 41–48. [CrossRef]
19. Waqar, M.; Sukmawati, R.; Ji, Y.; Sri Sumantyo, J. Tropical PeatLand Forest Biomass Estimation Using Polarimetric Parameters Extracted from RadarSAT-2 Images. *Land* **2020**, *9*, 193. [CrossRef]
20. Golshani, P.; Maghsoudi, Y.; Sohrabi, H. Relating ALOS-2 PALSAR-2 Parameters to Biomass and Structure of Temperate Broadleaf Hyrcanian Forests. *J. Indian Soc. Remote Sens.* **2019**, *47*, 749–761. [CrossRef]
21. Zeng, P.; Zhang, W.; Li, Y.; Shi, J.; Wang, Z. Forest Total and Component Above-Ground Biomass (AGB) Estimation through C- and L-Band Polarimetric SAR Data. *Forests* **2022**, *13*, 442. [CrossRef]
22. Gaveau, D.L.A. Modelling the Dynamics of ERS-1/2 Coherence with Increasing Woody Biomass over Boreal Forests. *Int. J. Remote Sens.* **2002**, *23*, 3879–3885. [CrossRef]
23. Chowdhury, T.A.; Thiel, C.; Schmullius, C. Growing Stock Volume Estimation from L-Band ALOS PALSAR Polarimetric Coherence in Siberian Forest. *Remote Sens. Environ.* **2014**, *155*, 129–144. [CrossRef]
24. Thiel, C.; Schmullius, C. The Potential of ALOS PALSAR Backscatter and InSAR Coherence for Forest Growing Stock Volume Estimation in Central Siberia. *Remote Sens. Environ.* **2016**, *173*, 258–273. [CrossRef]
25. Tebaldini, S. Single and Multipolarimetric SAR Tomography of Forested Areas: A Parametric Approach. *IEEE Trans. Geosci. Remote Sens.* **2010**, *48*, 2375–2387. [CrossRef]
26. Lei, Y.; Treuhaft, R.; Gonçalves, F. Automated Estimation of Forest Height and Underlying Topography over a Brazilian Tropical Forest with Single-Baseline Single-Polarization TanDEM-X SAR Interferometry. *Remote Sens. Environ.* **2021**, *252*, 112132. [CrossRef]
27. Solberg, S.; Hansen, E.H.; Gobakken, T.; Næssset, E.; Zahabu, E. Biomass and InSAR Height Relationship in a Dense Tropical Forest. *Remote Sens. Environ.* **2017**, *192*, 166–175. [CrossRef]
28. Lei, Y.; Lucas, R.; Siqueira, P.; Schmidt, M.; Treuhaft, R. Detection of Forest Disturbance With Spaceborne Repeat-Pass SAR Interferometry. *IEEE Trans. Geosci. Remote Sens.* **2018**, *56*, 2424–2439. [CrossRef]
29. Cloude, S.R.; Papathanassiou, K.P. Three-Stage Inversion Process for Polarimetric SAR Interferometry. *IEE Proc. Radar Sonar Navig.* **2003**, *150*, 125. [CrossRef]
30. Shi, Y.; He, B.; Liao, Z. An Improved Dual-Baseline PolInSAR Method for Forest Height Inversion. *Int. J. Appl. Earth Obs. Geoinf.* **2021**, *103*, 102483. [CrossRef]
31. Mao, Y.; Michel, O.O.; Yu, Y.; Fan, W.; Sui, A.; Liu, Z.; Wu, G. Retrieval of Boreal Forest Heights Using an Improved Random Volume over Ground (RVoG) Model Based on Repeat-Pass Spaceborne Polarimetric SAR Interferometry: The Case Study of Saihanba, China. *Remote Sens.* **2021**, *13*, 4306. [CrossRef]
32. Huang, Y.; Zhang, Q.; Ferro-Famil, L. Forest Height Estimation Using a Single-Pass Airborne L-Band Polarimetric and Interferometric SAR System and Tomographic Techniques. *Remote Sens.* **2021**, *13*, 487. [CrossRef]
33. Ter-Mikaelian, M.T.; Korzukhin, M.D. Biomass Equations for Sixty-Five North American Tree Species. *For. Ecol. Manag.* **1997**, *97*, 1–24. [CrossRef]
34. Wirth, C.; Schumacher, J.; Schulze, E.-D. Generic Biomass Functions for Norway Spruce in Central Europe—A Meta-Analysis Approach toward Prediction and Uncertainty Estimation. *Tree Physiol.* **2004**, *24*, 121–139. [CrossRef]
35. Hamdan, O.; Khali Aziz, H.; Mohd Hasmadi, I. L-Band ALOS PALSAR for Biomass Estimation of Matang Mangroves, Malaysia. *Remote Sens. Environ.* **2014**, *155*, 69–78. [CrossRef]
36. Neumann, M.; Saatchi, S.S. Polarimetric Backscatter Optimization for Biophysical Parameter Estimation. *IEEE Geosci. Remote Sens. Lett.* **2014**, *11*, 254–258. [CrossRef]
37. Bouvet, A.; Mermoz, S.; Le Toan, T.; Villard, L.; Mathieu, R.; Naidoo, L.; Asner, G.P. An Above-Ground Biomass Map of African Savannahs and Woodlands at 25 m Resolution Derived from ALOS PALSAR. *Remote Sens. Environ.* **2018**, *206*, 156–173. [CrossRef]
38. Vafaei, S.; Soosani, J.; Adeli, K.; Fadaei, H.; Naghavi, H.; Pham, T.; Tien Bui, D. Improving Accuracy Estimation of Forest Aboveground Biomass Based on Incorporation of ALOS-2 PALSAR-2 and Sentinel-2A Imagery and Machine Learning: A Case Study of the Hyrcanian Forest Area (Iran). *Remote Sens.* **2018**, *10*, 172. [CrossRef]

39. Shi, J.; Zhang, W.; Marino, A.; Zeng, P.; Ji, Y.; Zhao, H.; Huang, G.; Wang, M. Forest Total and Component Biomass Retrieval via GA-SVR Algorithm and Quad-Polarimetric SAR Data. *Int. J. Appl. Earth Obs. Geoinf.* **2023**, *118*, 103275. [CrossRef]
40. Englhart, S.; Keuck, V.; Siegert, F. Aboveground Biomass Retrieval in Tropical Forests—The Potential of Combined X- and L-Band SAR Data Use. *Remote Sens. Environ.* **2011**, *115*, 1260–1271. [CrossRef]
41. Loew, A.; Mauser, W. Generation of Geometrically and Radiometrically Terrain Corrected SAR Image Products. *Remote Sens. Environ.* **2007**, *106*, 337–349. [CrossRef]
42. Small, D.; Rohner, C.; Miranda, N.; Ruetschi, M.; Schaepman, M.E. Wide-Area Analysis-Ready Radar Backscatter Composites. *IEEE Trans. Geosci. Remote Sens.* **2022**, *60*, 1–14. [CrossRef]
43. Zhao, L.; Chen, E.; Li, Z.; Zhang, W.; Gu, X. Three-Step Semi-Empirical Radiometric Terrain Correction Approach for PolSAR Data Applied to Forested Areas. *Remote Sens.* **2017**, *9*, 269. [CrossRef]
44. Schuler, D.L.; Ainsworth, T.L.; Lee, J.S.; De Grandi, G. Topographic Mapping Using Polarimetric SAR Data. *Int. J. Remote Sens.* **1998**, *19*, 141–160. [CrossRef]
45. Iribe, K.; Sato, M. Analysis of Polarization Orientation Angle Shifts by Artificial Structures. *IEEE Trans. Geosci. Remote Sens.* **2007**, *45*, 3417–3425. [CrossRef]
46. Schuler, D.L.; Lee, J.-S.; De Grandi, G. Measurement of Topography Using Polarimetric SAR Images. *IEEE Trans. Geosci. Remote Sens.* **1996**, *34*, 1266–1277. [CrossRef]
47. Cloude, S.R.; Pottier, E. A Review of Target Decomposition Theorems in Radar Polarimetry. *IEEE Trans. Geosci. Remote Sens.* **1996**, *34*, 498–518. [CrossRef]
48. Lee, J.-S.; Schuler, D.L.; Ainsworth, T.L. Polarimetric SAR Data Compensation for Terrain Azimuth Slope Variation. *IEEE Trans. Geosci. Remote Sens.* **2000**, *38*, 2153–2163. [CrossRef]
49. Lee, J.-S.; Schuler, D.L.; Ainsworth, T.L.; Krogager, E.; Kasilingam, D.; Boerner, W.-M. On the Estimation of Radar Polarization Orientation Shifts Induced by Terrain Slopes. *IEEE Trans. Geosci. Remote Sens.* **2002**, *40*, 30–41. [CrossRef]
50. Wang, P.; Ma, Q.; Wang, J.; Hong, W.; Li, Y.; Chen, Z. An Improved SAR Radiometric Terrain Correction Method and Its Application in Polarimetric SAR Terrain Effect Reduction. *Prog. Electromagn. Res. B* **2013**, *54*, 107–128. [CrossRef]
51. Souissi, B.; Ouarzeddine, M. Polarimetric SAR Data Correction and Terrain Topography Measurement Based on the Radar Target Orientation Angle. *J. Indian Soc. Remote Sens.* **2016**, *44*, 335–349. [CrossRef]
52. Sun, G.; Ranson, K.J.; Kharuk, V.I. Radiometric Slope Correction for Forest Biomass Estimation from SAR Data in the Western Sayani Mountains, Siberia. *Remote Sens. Environ.* **2002**, *79*, 279–287. [CrossRef]
53. Atwood, D.K.; Andersen, H.-E.; Matthiss, B.; Holecz, F. Impact of Topographic Correction on Estimation of Aboveground Boreal Biomass Using Multi-Temporal, L-Band Backscatter. *IEEE J. Sel. Top. Appl. Earth Observ. Remote Sens.* **2014**, *7*, 3262–3273. [CrossRef]
54. Ulander, L.M.H. Radiometric Slope Correction of Synthetic-Aperture Radar Images. *IEEE Trans. Geosci. Remote Sens.* **1996**, *34*, 1115–1122. [CrossRef]
55. Small, D. Flattening Gamma: Radiometric Terrain Correction for SAR Imagery. *IEEE Trans. Geosci. Remote Sens.* **2011**, *49*, 3081–3093. [CrossRef]
56. Atwood, D.K.; Small, D.; Gens, R. Improving PolSAR Land Cover Classification With Radiometric Correction of the Coherency Matrix. *IEEE J. Sel. Top. Appl. Earth Observ. Remote Sens.* **2012**, *5*, 848–856. [CrossRef]
57. Castel, T.; Beaudoin, A.; Stach, N.; Stussi, N.; Le Toan, T.; Durand, P. Sensitivity of Space-Borne SAR Data to Forest Parameters over Sloping Terrain. Theory and Experiment. *Int. J. Remote Sens.* **2001**, *22*, 2351–2376. [CrossRef]
58. Hoekman, D.H.; Reiche, J. Multi-Model Radiometric Slope Correction of SAR Images of Complex Terrain Using a Two-Stage Semi-Empirical Approach. *Remote Sens. Environ.* **2015**, *156*, 1–10. [CrossRef]
59. Villard, L.; Le Toan, T. Relating P-Band SAR Intensity to Biomass for Tropical Dense Forests in Hilly Terrain: γ^0 or T^0? *IEEE J. Sel. Top. Appl. Earth Observ. Remote Sens.* **2015**, *8*, 214–223. [CrossRef]
60. Simard, M.; Riel, B.V.; Denbina, M.; Hensley, S. Radiometric Correction of Airborne Radar Images Over Forested Terrain With Topography. *IEEE Trans. Geosci. Remote Sens.* **2016**, *54*, 4488–4500. [CrossRef]
61. Georgopoulos, N.; Sotiropoulos, C.; Stefanidou, A.; Gitas, I.Z. Total Stem Biomass Estimation Using Sentinel-1 and -2 Data in a Dense Coniferous Forest of Complex Structure and Terrain. *Forests* **2022**, *13*, 2157. [CrossRef]
62. Rüetschi, M.; Schaepman, M.; Small, D. Using Multitemporal Sentinel-1 C-Band Backscatter to Monitor Phenology and Classify Deciduous and Coniferous Forests in Northern Switzerland. *Remote Sens.* **2017**, *10*, 55. [CrossRef]
63. Long, J.; Lin, H.; Wang, G.; Sun, H.; Yan, E. Mapping Growing Stem Volume of Chinese Fir Plantation Using a Saturation-Based Multivariate Method and Quad-Polarimetric SAR Images. *Remote Sens.* **2019**, *11*, 1872. [CrossRef]
64. Zhang, H.; Zhu, J.; Wang, C.; Lin, H.; Long, J.; Zhao, L.; Fu, H.; Liu, Z. Forest Growing Stock Volume Estimation in Subtropical Mountain Areas Using PALSAR-2 L-Band PolSAR Data. *Forests* **2019**, *10*, 276. [CrossRef]
65. Zhang, H.; Wang, C.; Zhu, J.; Fu, H.; Han, W.; Xie, H. Forest Aboveground Biomass Estimation in Subtropical Mountain Areas Based on Improved Water Cloud Model and PolSAR Decomposition Using L-Band PolSAR Data. *Forests* **2023**, *14*, 2303. [CrossRef]
66. Dostalova, A.; Navacchi, C.; Greimeister-Pfeil, I.; Small, D.; Wagner, W. The Effects of Radiometric Terrain Flattening on SAR-Based Forest Mapping and Classification. *Remote Sens. Lett.* **2022**, *13*, 855–864. [CrossRef]
67. Li, X.; Li, Y.; Zhang, J.; Peng, S.; Chen, Y.; Cao, Y. The Effects of Forest Thinning on Understory Diversity in China: A Meta-analysis. *Land Degrad. Dev.* **2020**, *31*, 1225–1240. [CrossRef]

68. Lu, H.; Zhang, H.; Fan, H.; Liu, D.; Wang, J.; Wan, X.; Zhao, L.; Deng, Y.; Zhao, F.; Wang, R. Forest Height Retrieval Using P-Band Airborne Multi-Baseline SAR Data: A Novel Phase Compensation Method. *ISPRS J. Photogramm. Remote Sens.* **2021**, *175*, 99–118. [CrossRef]
69. Fu, X.; Jiang, D.; Wang, L.; Gao, X.; Qian, D. Study on Biomass of *Larix-principis rupprechtiiin* Saihanba Mechanized Forestry Centre. *For. Ecol. Sci.* **2015**, *30*, 113–116. [CrossRef]
70. Jin, A. Study on the Biomass of the Main Trees at Bayingzhuang Forest Land in Hebei Province. Master's Thesis, Beijing Forestry University, Beijing, China, 2012.
71. Chu, C. Study on the Growth of Scotch Pine Plantations and the Variation of Soil Nutrients in Saihanba Aera. Master's Thesis, Hebei Agricultural University, Baoding, China, 2016.
72. Cao, J. Above- and Belowground Carbon Pools in Different Ages of Chinese Pine and Oriental Arborvitae Plantation Forests in Northern Mountain Areas of Beijing. Ph.D. Thesis, Beijing Forestry University, Beijing, China, 2011.
73. Yang, L. The Build Study of *Acer truncatum* Bunge Biomass Calculation Model in Western Hills of Beijing. Master's Thesis, Beijing Forestry University, Beijing, China, 2012.
74. Lee, J.-S.; Ainsworth, T.L. The Effect of Orientation Angle Compensation on Coherency Matrix and Polarimetric Target Decompositions. *IEEE Trans. Geosci. Remote Sens.* **2011**, *49*, 53–64. [CrossRef]
75. Liao, Z.; He, B.; Quan, X.; Van Dijk, A.I.J.M.; Qiu, S.; Yin, C. Biomass Estimation in Dense Tropical Forest Using Multiple Information from Single-Baseline P-Band PolInSAR Data. *Remote Sens. Environ.* **2019**, *221*, 489–507. [CrossRef]